

REPORT DOCUMENTATION PAGE

AFRL-SR-AR-TR-03-

0144

Public reporting burden for this collection of information is estimated to average 1 hour per response, including the time for reviewing instructions, gathering and maintaining the data needed, and completing and reviewing this collection of information. Send comments regarding this burden estimate or any other reducing this burden to Washington Headquarters Services, Directorate for Information Operations and Reports, 1215 Jefferson Davis Highway, Management and Budget, Paperwork Reduction Project (0704-0188), Washington, DC 20503.

| | | | |
|--|--|--|----------------------------|
| 1. AGENCY USE ONLY (Leave blank) | 2. REPORT DATE 21 Jan 2002 | 3. REPORT TYPE AND DURATION 01 Oct 1998 - 31 Dec 2001 | |
| 4. TITLE AND SUBTITLE Fundamental Theoretical and Numerical Issues of Turbulence in the Middle Atmosphere | | 5. FUNDING NUMBERS AFOSR G F49620-99-1-0300 | |
| 6. AUTHOR(S) Basil Nicolaenko Alex Mahalov | | 02-04-03A11:08 RCVD | |
| 7. PERFORMING ORGANIZATION NAME(S) AND ADDRESS(ES) Arizona State University Tempe, AZ 85287-1603 | | 8. PERFORMING ORGANIZATION REPORT NUMBER N/A | |
| 9. SPONSORING / MONITORING AGENCY NAME(S) AND ADDRESS(ES) Air Force Office of Scientific Research AFOSR/PKC 801 N. Randolph St., Room 732 Arlington, VA 22203-1977 | | 10. SPONSORING / MONITORING AGENCY REPORT NUMBER | |
| DISTRIBUTION STATEMENT A Approved for Public Release Distribution Unlimited | | | |
| 11. SUPPLEMENTARY NOTES | | 12a. DISTRIBUTION / AVAILABILITY STATEMENT Unrestricted Public Availability and Release | |
| | | 12b. DISTRIBUTION CODE | |
| 13. ABSTRACT (Maximum 200 Words) This project falls within the realm of the USAF Airborne Laser (ABL) Program. One of the challenges of the ABL program is the development of laser-beam propagation codes. Such codes must account for beam propagation through an extended turbulent medium of the bulk of the troposphere and stratosphere. From the operational perspective, accurate modeling of the refractive index structure function for long nearly horizontal path under high scintillation conditions characteristic of the atmosphere is important. Direct numerical simulations have been performed to study the dynamics of an inhomogeneous stratified shear flow modeling an atmospheric jet in the tropopause in the ABL context. The basic state is characterized by a jet at the tropopause in which the density stratification is vertically non-uniform. Small to moderate background stratifications are selected, and simulations are conducted for a range of Reynolds numbers. Quasi-equilibrium turbulent flow-fields are obtained by long-time integration of governing equations. The structure of the mean flow and turbulence fields are calculated and interpreted using relevant length scales. The jet core is found to support sustained mechanical (active) turbulence, outside of which lay a region of patchy turbulence and non-linear gravity wave activity characterized by spatially decaying velocity fluctuations and strong temperature fluctuations. | | | |
| 14. SUBJECT TERMS Atmospheric Turbulence, Optical Turbulence, Shear Stratified Flows, Optical Refractive Index Variability | | 15. NUMBER OF PAGES 48 16. PRICE CODE | |
| 17. SECURITY CLASSIFICATION OF REPORT UNCLASSIFIED | 18. SECURITY CLASSIFICATION OF THIS PAGE UNCLASSIFIED | 19. SECURITY CLASSIFICATION OF ABSTRACT UNCLASSIFIED | 20. LIMITATION OF ABSTRACT |

NSN 7540-01-280-5500

Standard Form 298 (Rev. 2-89)
Prescribed by ANSI Std. Z39-18
298-102

20030513 088

Final Report

**Fundamental Theoretical and Numerical Issues of
Characterization of Turbulence in the Middle
Atmosphere**

AFOSR Grant F49620-99-1-0300

B. Nicolaenko, Principal Investigator
A. Mahalov, Co-Principal Investigator

Departments of Mathematics
and
Program in Environmental Fluid Dynamics
Arizona State University
Tempe, AZ 85287-1804
e-mail: byn@stokes.la.asu.edu, mahalov@asu.edu

Synopsis

This project falls within the realm of the USAF mission of developing air defense systems, a component of which is the ongoing Airborne Laser (ABL) Program. The recent congressional mandate to develop an airborne missile defense system for the US will bolster the ABL program, since laser technology is a viable tool for such an effort. One of the major challenges of the ABL program is the development of laser-beam propagation codes. Such codes must account for the beam propagation through an extended turbulent medium of the bulk of the troposphere and stratosphere. From the operational perspective (Tactical Decision Aid Support), rigorous modeling of the refractive index structure function for long horizontal or nearly horizontal path under high scintillation conditions characteristic of the atmosphere is imperative. In spite of demonstrated importance of stratification on atmospheric optical turbulence, currently available ABL phase screen theories hinge upon isotropic Kolmogorov spectrum (Rytov's theory), and hence cannot represent large amplitude fluctuations of atmospheric stratified turbulence. In the context of such turbulence the collusion between the stratification and shear leads to many intriguing phenomena such as the formation of thin, elongated turbulent layers (pancakes) and instabilities (such as Kelvin-Helmholtz (K-H) billowing) that ultimately break down into turbulence. The turbulence so generated is often patchy and temporally intermittent, characterized by strong anisotropy. It produces strong optical scintillation due to refractive index fluctuations, which needs to be quantified accurately in developing beam control concepts for atmospheric laser-beam propagation.

In this project, direct numerical simulations have been performed to study the dynamics of an inhomogeneous stratified shear flow that models an atmospheric jet in the tropopause in the ABL context. The basic state is characterized by a jet centered at the tropopause in which the density stratification is vertically non-uniform. Small to moderate background stratifications are selected, and simulations are conducted for a range of Reynolds and Froude numbers. A spectral domain decomposition method that is particularly suitable for simulations of nonuniformly stratified shear flows is developed to generate the desired turbulent jet, and quasi-equilibrium flow-fields are obtained by long-time integration of governing equations. The structure of the mean flow and turbulence fields are calculated, which are interpreted using relevant length scales (Ozmidov, buoyancy, shear, Ellison) and Richardson number profiles. The ratios of the Ellison to buoyancy scales are much smaller than unity at the jet core and approach unity at the edges, confirming that mechanical turbulence prevails in the jet core, whereas nonlinear waves and stratification effects are significant at the edges. The jet core is found to support sustained mechanical (active) turbulence, outside of which lay a region of patchy turbulence and non-linear gravity wave activity characterized by spatially decaying velocity fluctuations and strong temperature fluctuations. Detailed energy budgets show how energy is partitioned within the flow, including the transport of

energy from the jet to its immediate vicinity by non-linear gravity waves. Applications include studies of the vertical variability of the optical refractive index function C_n^2 , which is of primary relevance to ABL propagation codes.

The following personnel has been supported by the grant:

- Prof. Alex Mahalov, Department of Mathematics and Mechanical & Aerospace Engineering, Center for Environmental Fluid Dynamics, Arizona State University
- Prof. Basil Nicolaenko, Department of Mathematics, and Center for Environmental Fluid Dynamics, Arizona State University
- Prof. HJS Fernando, Center for Environmental Fluid Dynamics, Arizona State University
- Dr. Binson Joseph, Post-Doctoral Fellow, Arizona State University
- Dr. Frank Tse, Post-Doctoral Fellow, Arizona State University
- Dr. Rafael Pacheco, Post-Doctoral Fellow, Arizona State University
- Prof. A. Babin, Collaborator, University of California, Irvine
- Doctoral students Markus Trahe and Bong-Sik Kim

Detailed Technical Report

1 Introduction

Some of the challenges in Air Borne Laser (ABL) performance predictions are tied to the effectiveness of propagation codes. The latter typically use discrete grids called phase screens to atmospherically induce phases to be simulated. Key questions in this process concern the number and size of screens, the grid spacing and the details of using atmospheric data and/or models to generate the field strengths at the grid points. Atmospheric variability generates spatial intermittency, non-stationarity in turbulence, which impacts on the variability of statistical characteristics of C_n^2 , the refractive index structure function. A fundamental characteristic of the middle atmosphere (tropopause and stratosphere) is stratification and layering: optical turbulence occurs in thin layers (pancakes or “blini”). The tropopause, by definition, is a region of sharp vertical temperature gradients at and above which stratification and layering are important; its altitudes vary from around 12 km at midlatitudes to 8 km in polar areas. The vertical extent of pancakes varies from 100–150 m to 30 m higher in the stratosphere. Balloon data show persistent, near constant altitude, layers of nearly 100 km horizontal extent. The extensive variability of the structure of the tropopause

considerably impacts on the structure of turbulence. There is a demonstrated need to better model atmospheric turbulence along long quasi-horizontal paths.

In the atmosphere, turbulence is generated by either convective or shear instabilities. In the middle atmosphere which is characterized by stable background stratification and shear, these instabilities and turbulence arise primarily from two sources:

- direct instabilities (such as shear at jet streams, convective plumes);
- gravity waves induced instabilities.

In the middle atmosphere stable background stratification and shear tend to influence motion scales that are larger than certain ‘outer’ scales (e.g. Ozmidov, buoyancy, Ellison). The scales of active Kolmogorov turbulence are those scales which are greater than the Kolmogorov scale but smaller than any outer scale. The Ozmidov scale is regarded as the outer scale above which the fluid turbulence is significantly affected by buoyancy. Also, the dynamics of a stably stratified turbulent flow depend on the rate at which fluid elements mix each other and change their density in the interior of the flow. The vertical displacements of the fluid elements are constrained by the amount of energy in the turbulence to lie within a buoyancy scale distance of the order of the buoyancy scale L_b . If the vertical velocity fluctuations due to internal waves are large compared to those due to turbulence, the buoyancy scale L_b is larger than L_o and vice versa. The scale L_e known as the overturning or Ellison scale uses the density fluctuations as an indicator of turbulent motions. The shear length scale L_s represents the lower bound of eddy sizes that are deformed by background shear, L_b is the buoyancy scale defined above and the scale L_d can be interpreted as the integral scale of embedded turbulence. When $L_d > L_s < L_b$ turbulence interacts with and extracts energy from the background shear, thus allowing the turbulent intensity to grow. The stratification can also interact with turbulence and shear, depending on the relative magnitudes of the scales L_s , L_b and L_d . For example, when $L_d < L_s < L_b$ the shear is expected to interact with stratification, thus producing instabilities (K-H billowing), gravity waves and intermittent (patchy) turbulence. When $L_b < L_d < L_s$ neither the instabilities nor shear-turbulence interactions may produce turbulence, and the existing turbulence in the flow is expected to decay.

Atmospheric variability generates spatial intermittency, non-stationarity in turbulence, which impacts on the variability of statistical characteristics of C_n^2 , the refractive index structure function. For classical homogeneous isotropic Kolmogorov turbulence, it is defined by $D_n(r) = C_n^2 r^{2/3}$, where $D_n(r)$ is the refractive index structure function in the inertial convective range:

$$D_n(r) = \langle (n(\mathbf{x}) - n(\mathbf{x} + \mathbf{r}))^2 \rangle,$$

where the bracket \langle , \rangle denotes ensemble averaging. The three-dimensional, nonstationary, intermittent, anisotropic structure of turbulence in the atmospheric field is coupled with

optical turbulence in thin layers (pancakes). Balloon measurements have been used to probe into the vertical structures of the atmosphere. Observations so obtained demonstrate the considerable impact of sharp vertical temperature gradients in the tropopause and the lower stratosphere and the extensive variability of the structure of the tropopause.

The following are some major issues regarding atmospheric turbulence impacting on ABL:

- Horizontal pancake turbulence has a very important impact on C_n^2 ; very little is experimentally known about the horizontal structure of turbulence and C_n^2 ;
- Very simple models such as CLEAR-1 and “onion skin” perform better than Rytov’s theory models but are still not adequate for turbulence realizations on phase screens in propagation codes;
- One needs 3D slew model that includes variability due to intermittency, nonstationarity and stratification (vary C_n^2 appropriately);
- Modeling anisotropic C_n^2 along paths spanning whole pancakes as well as the strong shearing domains between pancakes is an intricate issue that need to be investigated by probing into the structure of pancakes;
- Weather front dynamics also impact via intense velocity shearing on strong variability of C_n^2 .

In this project we have focused on investigating turbulence in a non-homogeneous stratified shear flow where the velocity profile takes the form of a jet (cf. figure 1). In the upper troposphere and stratosphere localized regions of three-dimensional turbulence arise through shear instability or through breaking of inertia-gravity waves. Upper-level atmospheric jet regions are also strongly influenced by stable background stratification (cf. figure 2). The flow belongs to the class of nonuniformly stratified (with a doubling of buoyancy frequency across the jet) shear flows, whose turbulence characteristics are not well-understood. We set up our model based on jet streams encountered in the Earth atmosphere at the tropopause. This region corresponds to the transition between the tropopause and the stratosphere which one observes at an altitude about 10 to 15 km depending on the latitude. We consider a nonuniformly stratified jet centered at the vertical coordinate $z = 0$. The flow consists of a jet core surrounded by two shear layers; the layer above has a negative shear and a stronger temperature gradient, while the layer below has a positive shear and presents a weaker temperature gradient, with the buoyancy (Brunt-Väisälä) frequency being reduced by a factor of two. This latter configuration is typical of the jet streams in the tropopause (cf. figures 1 and 2).

The gradient Richardson number, which quantifies stratification and shear effects, is low within the jet core (except at the very center) and velocity fluctuations are maximal there, thus providing sustained turbulence (cf. figures 3a and 3b). It increases towards the jet edges

where the effect of stratification tends to reduce turbulence with the shear length scale exceeding the buoyancy outer scale. Tropopausal turbulence, driven by shear instabilities on either side of the jet axis, results in mean stratification with a notch in Brunt-Väisälä frequency profile, a configuration favoring gravity wave emission. The flow in the vicinity of the edges of the jet is locally out of equilibrium and, in particular, produces nonlinear gravity waves which travel further away and break ([Sutherland & Peltier (1995)]). Regions far from the jet edges have weaker velocity fluctuations than in the core, and hence meager turbulent mixing, although potential energy and temperature fluctuations remain appreciable. The above scenarios are in agreement with aircraft observations of [Bedard, Canavero & Einaudi (1986)]. Critical levels where waves extract energy from the mean flow correspond to those regions of enhanced turbulence, where the Richardson number is below 0.25, hence generating Kelvin-Helmholtz instabilities ([Kaltenbach, Gerz & Schumann (1994)]).

Our focus is on the dynamics and vertical variability of scales that are poorly resolved in mesoscale meteorological codes such as MM5 and WRF ([Grell, Dudhia & Stauffer (1995)]). Such knowledge is important not only for parameterization and modeling of tropopausal turbulence and associated mixing in mesoscale models under stably stratified conditions (above the atmospheric boundary layer), but also for determining refractive index structure functions pertinent to electromagnetic wave propagation across the tropopause ([Beland (1993)]; [Eaton & Nastrom (1998)]; [Nastrom, Gage & Ecklund (1986)]; [Dalaudier, Sidi, Crochet & Vernin (1994)]). Vertical scales controlling the size of ‘sheets’ in the atmospheric temperature field have been directly evidenced by the analysis of field measurements; the main dynamical properties of such layers, whether strongly mixed or ‘calm’, can be characterized not only by the gradient Richardson number but also by various outer scales of turbulence ([Alisse & Sidi (2000)]). We investigate how the dynamics and dominant physical processes in the stratified jet are reflected in various length scales. In particular, we study vertical variability of outer scales and their dependence on the background synoptic scale jet stream and the background Brunt-Väisälä profile across the tropopause. Beyond a sufficient threshold of resolution (especially in the vertical direction) our DNS simulations demonstrate saturation with increased numerical resolution of the vertical variability curves for *ratios* of various outer scales; cf. figure 3b for $Ri_g = L_s^2/L_b^2$ and figure 23b for the temperature fluctuation parameter L_e/L_b , where L_s is the shear scale, L_b is the buoyancy scale and L_e is the Ellison scale. These resolution independent ratios are an effective gauge of the variability of inhomogeneous mixing in a nonuniformly stratified tropopause jet.

Only a very few studies have been reported with regard to three-dimensional, high-resolution numerical simulations that employ realistic models of the nonuniformly stratified

tropopause jet. [Sutherland & Peltier (1995)] and [Smyth & Moum (2002)] implemented a jet-like velocity profile as the initial condition; the Brunt-Väisälä profiles used in their model was also doubled from the lower to the upper domains. However, their simulations are only two dimensional and the jet profiles tend to be smeared as there is no sustained momentum source in their model, which caused the shear to steadily decrease. In the atmosphere, on the other hand, the jet is maintained quasi-steady by the synoptic scale forcing, which needs to be considered in modeling. It should be noted that there are many numerical studies of stratified turbulent shear flows, which impose a constant mean shear and stratification in the vertical direction. The horizontal directions are then regarded as periodic and the vertical direction shear periodic. The work by [Gerz, Schumann & Elghobashi (1989)]; [Holt, Koseff & Ferziger (1992)]; [Kaltenbach, Gerz & Schumann (1994)], [Carnevale, Briscoline & Orlandi (2001)] and [Jacobitz, Sarkar & Van Atta (1997)] belong to this category. Turbulent flows with mean shear and stratification are typically temporally evolving and hence do not reach stationary states, except at a certain ‘stationary’ Richardson number for which the production is balanced by the dissipation. Asymptotic stationary states can be attained, however, where normalized variables (e.g. ratios of individual components of energy to total energy) reach constant values after several turnover periods. Another approach in the study of shear-stratified turbulence uses decaying simulations. An example is the DNS studies of [Galmiche, Thual & Bonneton (2002)] dealing with non-uniform vertical mean shear and non-uniform stratification, where mean velocity and density profiles are allowed to evolve with time. In such simulations, however, the flow does not reach equilibrium and it remains unclear whether the results are sensitive to the generally transient nature of the flow.

While previous numerical studies have made important contribution to the study of shear-stratified turbulence, they do not reproduce exact middle atmospheric situation: wherein the turbulence can reach some quasi-equilibrium state and where the turbulent kinetic energy (TKE) budgets are nearly balanced. Furthermore, if homogeneous boundary conditions are used in the vertical direction, there is no net heat and momentum transfer out of the box. As we demonstrate in Section 3, the fluxes play an important role in redistributing energy in the vertical direction. Without such a mechanism, the variability of the atmospheric turbulence around the jet cannot be reproduced. It has been shown in [Sutherland & Peltier (1995)] that the momentum flux created from the jet produces internal (i.e. non-topographical) gravity waves which in turn produce a drag on the mean velocity. These phenomena cannot be reproduced by conventional shear periodic numerical experiments, the application of which to atmospheric tropopause simulations in the presence of a jet stream is thus limited.

Our model of the atmospheric tropopause is characterized by a stratified thin layer across which the buoyancy frequency jumps approximately by a factor of two (figure 2). In our three-dimensional direct numerical simulations (DNS), the streamwise velocity profile that characterizes the basic state of the model jet was set to a gaussian profile, thus producing shear at different vertical levels characteristic of a jet stream. The governing equations are solved for the above flow configuration using DNS based on a spectral domain technique developed specifically for flows characterized by non-uniform background shear and stratification ([Tse, Mahalov, Nicolaenko & Fernando (2001)]). Due to inhomogeneity in the vertical direction, periodic boundary conditions are not used therein; previous numerical studies have assumed such periodicity. In our simulations, non-linear shear and stratification profiles adjust to roughly stationary values, around which the potential and kinetic energies fluctuate. Quasi-equilibrium solutions are obtained following long-time integration of governing equations. The robustness of our results has been verified by DNS at doubled resolution (1024 vertical levels). Thus, physical results reported here and, in particular, those involving ratios of outer scales are resolution independent. We investigate the effects of inhomogeneity of shear and stratification, especially those properties that are distinct from homogeneous stratified shear flows.

The next section describes the computational framework for non-homogeneous stratified shear flows. Section 3 presents the results of numerical simulations and discussions of various mean quantities and variances at quasi-equilibrium. Vertical variability of natural length scales (Ozmidov, buoyancy, shear and Ellison) and Richardson number profiles are analyzed in Section 4. Turbulent budget equations are investigated in Section 5. Conclusions and issues for future work are discussed in Section 6.

2 Computational framework for non-homogeneous stratified shear flows

2A Description of numerical experiments

The governing equations are the three-dimensional incompressible Navier-Stokes equations for the velocity \mathbf{U} and temperature Θ under the Boussinesq approximation:

$$\frac{\partial \mathbf{U}}{\partial t} + \mathbf{U} \cdot \nabla \mathbf{U} = -\frac{\partial P}{\partial x} + \nu \nabla^2 \mathbf{U} + \Pi_U, \quad (2.1)$$

$$\frac{\partial V}{\partial t} + \mathbf{U} \cdot \nabla V = -\frac{\partial P}{\partial y} + \nu \nabla^2 V, \quad (2.2)$$

$$\frac{\partial W}{\partial t} + \mathbf{U} \cdot \nabla W = -\frac{\partial P}{\partial z} + \nu \nabla^2 W + g\beta(\Theta - \Theta_R), \quad (2.3)$$

$$\frac{\partial \Theta}{\partial t} + \mathbf{U} \cdot \nabla \Theta = \kappa \nabla^2 \Theta + \Pi_\Theta, \quad (2.4)$$

$$\nabla \cdot \mathbf{U} = 0, \quad (2.5)$$

where $\mathbf{U} = (U, V, W)$ are the three components of the velocity in the streamwise, spanwise and vertical directions (denoted as x, y, z) respectively, Θ_R is the constant reference temperature; P is the pressure; ν , κ , β and g are the molecular viscosity, molecular diffusivity, thermal expansion coefficient and gravitational acceleration, respectively. The horizontally homogeneous terms Π_U and Π_Θ are the vertically dependent momentum and thermal sources. The two source terms enable to obtain a basic (unstable) jet stream profile and a desired vertically variable Brunt-Väisälä frequency profile. They represent large scale momentum and thermal forcing responsible for maintaining the jet.

From now on, the total instantaneous variables are represented by upper case letters (U, V, W, Θ). They are decomposed into two parts : basic state and perturbations. The variables in the basic state are represented by upper case letters with subscripts (U_b and $\Theta_R + \Theta_b$), and perturbations by lower case letters (u, v, w, θ). The perturbation is further decomposed into two components: a mean (horizontally averaged) part denoted by $\langle \cdot \rangle$ and a fluctuating component denoted by primes. Thus, the variables U, V, W, Θ are decomposed as :

$$U = U_b(z) + u(x, y, z, t) = U_b(z) + \langle u \rangle(z, t) + u'(x, y, z, t), \quad (2.6)$$

$$V = v(x, y, z, t) = \langle v \rangle(z, t) + v'(x, y, z, t), \quad (2.7)$$

$$W = w(x, y, z, t) = w'(x, y, z, t), \quad (2.8)$$

$$\Theta = \Theta_R + \Theta_b(z) + \theta(x, y, z, t) = \Theta_R + \Theta_b(z) + \langle \theta \rangle(z, t) + \theta'(x, y, z, t). \quad (2.9)$$

We have $\langle u' \rangle = \langle v' \rangle = \langle w' \rangle = 0$. The mean (horizontally averaged) values of U and Θ contain a part from the basic state and a part from the perturbation (e.g. $\bar{U} = U_b + \langle u \rangle$), while the mean of V satisfies ($\bar{V} = \langle v \rangle$). The pressure can also be decomposed as :

$$P = P_b(z) + p(x, y, z, t) = P_b(z) + \langle p \rangle(z, t) + p'(x, y, z, t). \quad (2.10)$$

For the basic state, where the perturbations u, v, w and θ are zero and the fields depend only on z , the governing equations are reduced to :

$$\Pi_U + \nu \frac{\partial^2 U_b}{\partial z^2} = 0, \quad (2.11)$$

$$\frac{\partial P_b}{\partial z} = g\beta\Theta_b, \quad \Pi_\Theta = -\kappa \frac{\partial^2 \Theta_b}{\partial z^2}. \quad (2.12)$$

Here Π_U is obtained by assigning to U_b the following gaussian form:

$$U_b(z) = U_b(0) e^{-(\alpha_1 z)^2} e^{-\left(\frac{L_z}{L_z-z}\right)^2} e^{-\left(\frac{L_z}{L_z+z}\right)^2} e^2, \quad (2.13)$$

where α_1 is the stiffness parameter and L_z is the half depth of the computational box. The velocity profile $U_b(z)$ is equal to $U_b(0)$ at the center. The momentum source Π_U and the thermal source Π_Θ are obtained from eq. (2.11) and from eq. (2.12), respectively. The momentum source is intended to maintain a sustained synoptic/planetary jet stream in the model (figure 1). The thermal source maintains the mesoscale doubling of the buoyancy frequency across the tropopause. Thus, we are resolving a microscale box centered on a synoptic-scale jet stream at the tropopause, for times much shorter than time scales of jet dynamics. The jet profile for U_b is shown in figure 1b, with $\alpha = \alpha_1 = 16$. This profile models the measured wind profile of an atmospheric jet shown in figure 1a.

In eq. (2.12), the buoyancy force due to background temperature gradient is balanced by the basic state pressure, the thermal source is balanced by the diffusion of the background temperature. Substituting eq. (2.9), (2.10) and (2.12) into eq. (2.3) - (2.4), the equations for vertical velocity and temperature can then be expressed as :

$$\frac{\partial W}{\partial t} + \mathbf{U} \cdot \nabla W = -\frac{\partial p}{\partial z} + g\beta\theta + \nu\nabla^2 W, \quad (2.14)$$

$$\frac{\partial \theta}{\partial t} + \mathbf{U} \cdot \nabla \theta = -W \frac{\partial \Theta_b}{\partial z} + \kappa\nabla^2 \theta, \quad (2.15)$$

where β is the thermal expansion coefficient. Next, let $N^2 K^2(z) = g\beta\partial\Theta_b(z)/\partial z$ and $\vartheta = g\beta\theta/N$ where N is a constant (N^{-1} has the unit of time) and $K(z)$ is a vertical profile factor, we obtain the rescaled vertical velocity and temperature equations (e.g. [Herring & Metais (1989)]):

$$\frac{\partial W}{\partial t} + \mathbf{U} \cdot \nabla W = -\frac{\partial p}{\partial z} + N\vartheta + \nu\nabla^2 W, \quad (2.16)$$

$$\frac{\partial \vartheta}{\partial t} + \mathbf{U} \cdot \nabla \vartheta = -WNK^2 + \kappa\nabla^2 \vartheta. \quad (2.17)$$

The variable ϑ has the unit of length/time (not to be confused with θ which has the unit of temperature). In the above equation N and $K(z)$ are related to the usual Brunt-Väisälä frequency profile $\mathcal{N}^2(z) = \frac{g}{\Theta} \frac{\partial \Theta}{\partial z}$ as:

$$N^2 K^2(z) = g\beta \frac{\partial \Theta_b}{\partial z} = \beta\Theta \mathcal{N}^2(z). \quad (2.18)$$

In our simulations, the non-dimensional $K(z)$ profile has the following form:

$$K(z) = 1 + \frac{1}{e^{-\alpha_2 z} + 1}. \quad (2.19)$$

The profile $K(z)$ corresponds to a temperature profile which increases monotonically from the bottom to the tropopause level, experiences a stiff transition at the tropopause which

depends on the stiffness parameter α_2 , then further increases reaching at the top twice the value at the bottom. This dimensionless profile models the doubling of Brunt-Väisälä frequency at the tropopause, as observed in balloon field measurement by [Beland (1993)], figure 2 (doubling roughly from 0.01s^{-1} to 0.02s^{-1}). Equations (2.13) and (2.19) introduce two parameters α_1 and α_2 , which specify the inverse of the external length scales of the system. The first number α_1 controls the amount of shear along the jet edges while the second parameter α_2 controls the stiffness in Brunt-Väisälä profile. In our simulations, the same values are used for α_1 and α_2 ($\alpha = \alpha_1 = \alpha_2 = 16$). The edges of the jet are then located in the vicinity of the normalized vertical levels $z\alpha \approx \pm 1$.

The variables can be non-dimensionalized by choosing a suitable velocity scale $U_\alpha = U_b(0)$ and length scale L_α . We define $L_\alpha = 1/\alpha$ and $\tilde{z} = \alpha z = z/L_\alpha$. Hence, in terms of the rescaled \tilde{z} and with $\alpha = 16$, the computational box corresponds to $-5.0 \times 16 \leq \tilde{z} \leq 5.0 \times 16$. Similarly, we rescale $\tilde{x} = \alpha x$, $\tilde{y} = \alpha y$, with $0 \leq \tilde{x}, \tilde{y} \leq 8\pi$. The nondimensionalized equations then become :

$$\frac{\partial \tilde{U}}{\partial \tilde{t}} + \tilde{\mathbf{U}} \cdot \nabla \tilde{U} = -\frac{\partial \tilde{P}}{\partial \tilde{x}} + \frac{1}{Re_0} \tilde{\nabla}^2 \tilde{U} + \tilde{\Pi}_U, \quad (2.20)$$

$$\frac{\partial \tilde{V}}{\partial \tilde{t}} + \tilde{\mathbf{U}} \cdot \nabla \tilde{V} = -\frac{\partial \tilde{P}}{\partial \tilde{y}} + \frac{1}{Re_0} \tilde{\nabla}^2 \tilde{V}, \quad (2.21)$$

$$\frac{\partial \tilde{W}}{\partial \tilde{t}} + \tilde{\mathbf{U}} \cdot \nabla \tilde{W} = -\frac{\partial \tilde{P}}{\partial \tilde{z}} + \frac{1}{Re_0} \tilde{\nabla}^2 \tilde{W} + \frac{1}{Fr} \tilde{\vartheta}, \quad (2.22)$$

$$\frac{\partial \tilde{\vartheta}}{\partial \tilde{t}} + \tilde{\mathbf{U}} \cdot \nabla \tilde{\vartheta} = -\frac{1}{Fr} \tilde{W} K^2 + \frac{1}{Re_0 Pr} \tilde{\nabla}^2 \tilde{\vartheta}, \quad (2.23)$$

leaving only three dimensionless parameter groups in the equations: the Froude number $Fr = U_\alpha/NL_\alpha$, initial Reynolds number $Re_0 = U_\alpha L_\alpha/\nu$ and Prandtl number $Pr = \nu/\kappa$. Similarly, the source now has the form :

$$\tilde{\Pi}_U = -\frac{1}{Re_0} \frac{\partial^2 \tilde{U}_b}{\partial \tilde{z}^2}, \quad (2.24)$$

where

$$\tilde{U}_b(\tilde{z}) = e^{-\tilde{z}^2} e^{(\frac{L_z \alpha}{L_z \alpha - \tilde{z}})^2} e^{(\frac{L_z \alpha}{L_z \alpha + \tilde{z}})^2} e^2. \quad (2.25)$$

The governing equations (2.1), (2.2), (2.16) and (2.17) are solved using numerical methods described in Section 2.2. The parameters for this problem are κ , ν , $U_b(0)$, N , and α ; their values used in our simulations are listed in table 1. Case 1 is regarded as the reference case. The viscous and thermal diffusivities are set to 1×10^{-4} and 1.4×10^{-4} , respectively, for cases 1-5 and 6×10^{-5} and 8.6×10^{-5} for case 6, resulting in a Prandtl number ν/κ of 0.7 in all cases as for air. Case 2 has higher and case 3 has lower stratification compare to

Table 1: Physical parameters used in simulations with $\nu = 1 \times 10^{-4}$, $\kappa = 1.4 \times 10^{-4}$ (cases 1-5) and $\nu = 6 \times 10^{-5}$, $\kappa = 8.6 \times 10^{-5}$ (case 6). $Pr = 0.7$ in all cases.

| Case | $U_b(0)$ | resolution | $Re_0 = \frac{U_b}{\nu\alpha}$ | N |
|------|----------|---------------------|--------------------------------|------|
| 1 | 4 | $128^2 \times 512$ | 2500 | 0.2 |
| 2 | 4 | $128^2 \times 512$ | 2500 | 1.0 |
| 3 | 4 | $128^2 \times 512$ | 2500 | 0.05 |
| 4 | 10 | $256^2 \times 512$ | 6250 | 0.2 |
| 5 | 20 | $256^2 \times 512$ | 12500 | 0.2 |
| 6 | 20 | $512^2 \times 1024$ | 20833 | 0.2 |

case 1. The dependence on stratification can be studied through the first three cases. Cases 4, 5 and 6 have higher forcing respectively, as evident of their respective Reynolds numbers. Cases 4 and 5 are simulated with a resolution of $256^2 \times 512$ while cases 1-3 have a resolution of $128^2 \times 512$. The largest Reynolds number simulation in case 6 has the highest resolution of $512^2 \times 1024$.

The vertical gradient of $U_b(z)$ is large in the middle region (except at $z = 0$) and correspondingly $Ri_g = (NK(z))^2/(dU_b/dz)^2$ is small there. The base jet profile is linearly unstable ($Ri_g < 0.25$). The shear is sufficiently large to overcome the stability due to stable stratification and the flow develops instabilities and turbulence. Based on the centerline velocity of the jet at the basic state $U_b(0)$ and α^{-1} , the initial Reynolds number is given in table 1. Case 1, 2 & 3 have the same Reynolds number but different background stratification. Increasing the forcing parameter has the effect of increasing the Reynolds number (cases 4, 5 and 6). For the quasi-equilibrium turbulent state we define turbulent length and velocity scales as follows. The lengthscale, $L_d = q^3/\epsilon$ is based on the turbulent kinetic energy (TKE) dissipation ϵ and q ([Batchelor (1953)]):

$$\epsilon = \nu \langle s_{ij} s_{ij} \rangle, \quad q^2 = \langle u'^2 + v'^2 + w'^2 \rangle, \quad (2.26)$$

where $s_{ij} = 1/2(\partial u_i / \partial x_j + \partial u_j / \partial x_i)$ is the rate-of-strain tensor ([Pope (2000)]) and u_i and x_i ($i = 1, 2, 3$) correspond to our u, v, w and x, y, z notation respectively. The values of turbulent Reynolds number Re_d and Froude number Fr_d with this set of scales are given in table 2 for the vertical level $\alpha z = 1.0$. The scales and the Reynolds number Re_d vary

Table 2: Values of parameter groups at quasi-equilibrium at the vertical level $\alpha z = 1.0$; Froude $Fr_d = \frac{q}{N_{eq} L_d}$ and Reynolds $Re_d = \frac{q L_d}{\nu}$ numbers are based on the length scale L_d .

| Case | 1 | 2 | 3 | 4 | 5 | 6 |
|--------|------|------|------|------|------|------|
| Fr_d | 1.26 | 0.41 | 5.21 | 1.98 | 2.54 | 1.11 |
| Re_d | 826 | 534 | 798 | 1392 | 2392 | 4016 |

with vertical levels, being highest near the edges of the jet and decay rapidly away from the edges; see figure 4 for case 6 with $512 \times 512 \times 1024$ resolution.

2B Numerical methods

Most of the previous numerical simulations of shear-stratified turbulence have been in the context of uniform background stratification or uniform shear. In the present study we use a spectral domain decomposition method, which is particularly suitable for simulation of flows with non-uniform background stratification and shear. The flow is assumed to be homogeneous only in the horizontal directions where periodic boundary conditions are used. For each horizontal wavenumber, the vertical domain is then broken down into several subdomains (figure 5). Each subdomain is separately mapped to a domain $\{-1 \leq z' \leq 1\}$. For non-overlapping subdomains, there are basically two solution methods: collocation and variational methods. In the collocation method, the variable (e.g. λ) within each subdomain j is interpolated as :

$$\lambda^j(z') = \sum_{i=0}^n c_i^j \phi_i(z'), \quad -1 \leq z' \leq 1, \quad (2.27)$$

where n is the order of interpolation, and the functions $\phi_i(z')$ are the Lagrange interpolants. The local coordinate z' is chosen to be the Gauss Lobatto Legendre points.

The differentiation of variables are carried out by differentiating the interpolants. Efficient routine for the differentiation exists, e.g. [Fornberg (1996)]. Domain decomposition method, however, requires patching of subdomain boundaries when forming the global differentiation matrix. In inverting the 2nd order differentiation matrix (e.g. in calculating the pressure Poisson equation), continuity of the 1st order derivative is required as subdomain boundary condition. This is usually done by replacing $n - 1$ rows (corresponding to $n - 1$ subdomain boundaries) of the global matrix by the 1st order derivative equations. This

method, however, may lead to numerical disturbances at the subdomain boundaries, particularly if the resolution of the problem is marginal. To overcome this problem, an auxillary set of subdomains is defined, with each subdomain in the auxillary set strides across the sub-domains in the primary set. The arrangement is shown schematically in figure 5. Another global differentiation matrix is formed. Differentiation or integration are then carried out by multiplication or inversion of a combination of these two matrices. When this method is used in advection-diffusion equation, exponential convergence of accuracy is observed for increasing order of interpolation. The method has been tested for the turbulent channel flow problems, and excellent performance has been noted. Further details on the numerical method are given in [Tse, Mahalov, Nicolaenko & Fernando (2001)].

The time discretization follows the usual pressure projection method, which separates the time derivatives into three substeps. The nonlinear terms and buoyancy terms are advanced in the first substep; pressure Poisson equations are then solved directly and the pressure terms are advanced in the second substep while the dissipation term is considered in the third. Second order Adams-Bashforth scheme is used for the nonlinear terms. The calculation of derivatives involved in the nonlinear terms is carried out in physical space using collocation methods. The third substep requires calculating the viscous terms implicitly. A total of eight forward FFT transforms and four backward FFT transforms is required. In the vertical direction, absorption layers are added to the top and bottom boundaries to remove, or at least reduce, reflection of waves. The length of the computational box shown in figure 5b is $\pi/2$ in horizontal directions and from -5.0 to $+5.0$ in the vertical direction. Grid resolution in our work includes $128 \times 128 \times 512$, $256 \times 256 \times 512$ and $512 \times 512 \times 1024$ (table 1). There are 127 (for cases 1-5) and 255 (for case 6) subdomains vertically. The interpolation for the central three subdomains is 5th order while for the rest is 4th order. The total number of grid points in the vertical is then power of two, avoiding one processor carrying an extra plane for computation. The width of the subdomains between -0.062 to 0.062 is 0.004, and it gradually increases to 0.2 at the outer region. The jet stream is placed in the center of the computational domain. This region requires more resolution due to high shear (figure 5). The program is parallelized by the transposition method using MPI. Typically, for resolution of $128 \times 128 \times 512$, it takes 15 seconds to advance one time step on a cluster of 32 SGI R10000 processors and for $512 \times 512 \times 1024$ resolution, it takes ≈ 5 minutes on 128 processors. The computations are done on the Nirvana massively parallel supercomputer at Los Alamos National Laboratory and the DoD ARL MSRC.

2C Quasi-equilibrium state

Long time integration of the governing eqs. (2.1) - (2.5) is affected by the presence of adiabatic invariants for the long time dynamics. In particular, it has been shown in [Babin, Mahalov & Nicolaenko (1998)] that in the asymptotic state (after several periods of oscillations associated with wave motions; [Mahalov, Nicolaenko & Zhou (1998)]) the horizontally averaged temperature $\langle \vartheta \rangle$ is a near adiabatic invariant with only a small drift in time; this drift is confirmed by figure 6 in our DNS. We recall the mean (horizontally averaged) temperature equations:

$$\frac{\partial \langle \vartheta \rangle}{\partial t} + \frac{\partial \langle w' \vartheta' \rangle}{\partial z} = \kappa \frac{\partial^2 \langle \vartheta \rangle}{\partial z^2}. \quad (2.28)$$

A state of absolute equilibrium is one where the mean temperature $\langle \vartheta \rangle$ as well as other (horizontally) averaged quantities are no longer changing with time. We define quasi-equilibrium to be a state where $\langle \vartheta \rangle$ satisfies eq. (2.28) with a small but finite time derivative (slow steady drift as in figure 6); and where all other means are quasi-stationary and the integrated statistics of variances show little fluctuation (< 5%). This is illustrated in figure 7 for a typical case where the vertically integrated values of velocity variances, $\int \langle u'^2 \rangle dz$ (I), $\int \langle v'^2 \rangle dz$ (II) and $\int \langle w'^2 \rangle dz$ (III), temperature variance $\int \langle \vartheta'^2 \rangle dz$ (IV) and the rate of change of horizontal velocity variance, $\int |\partial \langle u'^2 \rangle / \partial t| dz$ (V), are plotted against the large eddy overturning time ($S_b^{-1} = (\max |\partial U_b / \partial z|)^{-1} \approx 0.018$). Our range for $S_b t$ is longer than those reported in homogeneous simulations since we are using the maximum value of shear at basic state. The actual shear increases from zero to the quasi-equilibrium values and also depends on the vertical level. All the curves initially overshoot and then settle down to a relatively constant value. The first stage of evolution corresponds to the onset of Kelvin-Helmholtz instabilities. Secondary instabilities then kick-in, with transition to 3D turbulence and the values of the variances drop and begin to saturate. The same trend has been observed, for example, in [Smyth & Moum (2000)]. After the velocity variances become quasi-stationary, the horizontally averaged mean temperature is still evolving, albeit slowly, as shown in figure 6 for case 1. Physically, quasi-equilibrium states can be obtained if the synoptic scale driving force has a much longer time scale (e.g. see figure 3 of [Cullen (2002)]). The turbulence so obtained is in local equilibrium with TKE production in large scales which dissipates at smaller scales. This is evident from the spectra in quasi-equilibrium state presented in [Tse, Mahalov, Nicolaenko & Fernando (2001)], which span several decades.

3 The mean profiles, variances and covariances

In this section, based on our long-time DNS, we present vertical profiles at quasi-equilibrium for the mean temperature, three velocity components and the corresponding variances and co-

variances. The mean (horizontal averaged) velocity in the streamwise direction $\bar{U} = U_b + \langle u \rangle$ at quasi-equilibrium is shown in figure 8 for the cases from table 1. Those figures are time-averaged for one large eddy turnover time defined by $2\pi/(\alpha g)$. The vertical axis is nondimensionalized by $1/\alpha$ and the velocity is non-dimensionalized by $\bar{U}(0)$. Hence the normalized values are all equal to unity at the center. Cases 1, 2 and 3 are shown in figure 8a while cases 4, 5 and 6 are shown in figure 8b. The profiles for cases 5 and 6 are essentially identical. The amount of stratification does not have much effect on the width of the mean flow, which is dictated by the profile of the momentum source Π_U . There is a counter flow away from the central region. Note that the asymmetry generated by the doubling of the Brunt-Väisälä profile, is more prominent in case 2 than in the other cases. The peak value of $\bar{U} = U_b + \langle u \rangle$ in this case is also larger than in other cases. In the decaying simulation by [Galmiche, Thual & Bonneton (2002)], an increase of stratification has been observed to cause transfer of energy from turbulence to the mean. Apparently, we encounter a similar situation in our quasi-equilibrium simulations.

The mean temperature profiles $\langle \vartheta \rangle$, which is the mean of the perturbation of the basic profile, is a slowly evolving quantity that can serve as an indicator of a particular quasi-equilibrium state at that vertical level. Their graphs are plotted in figure 9, with values normalized by $\bar{U}(0)$ (ϑ has the unit of velocity). The values are negative in the upper domain and positive in the lower domain. As will be seen later in figure 20, the vertical heat flux is negative in the central region and it is very small elsewhere. As a result, the temperature decreases at the top and increases at the bottom due to buoyancy flux crossing the center. In figure 9 the peaks for case 2 are the largest, followed by case 1 while case 3 has the smallest peaks. One prominent feature is that, as the stratification decreases, the peaks move away from the core of the flow. Consider case 3 for example, $\langle \vartheta \rangle$ peaks at $z\alpha \approx 5.36$ and -4.96 , at distances significantly away from the sides of the jet at $z\alpha \approx \pm 1$. There are no significant differences in the location of peaks for cases 4, 5 and 6.

Figure 10a shows profiles of the turbulent mean state squared Brunt-Väisälä (buoyancy) frequency (N^2). A dramatic decrease of N^2 in the jet core, through turbulent dynamics and mixing, is clearly noticed (it takes negative values in case 3 for some vertical levels implying the existence of unstably stratified layers). A N^2 profile of this kind, with a localized minimum in the mixing region, is sometimes referred to as possessing a ' N^2 notch'. It is known to be a mean state configuration favoring emission of gravity waves from tropospheric jet streams ([Lott, Kelder & Teitelbaum (1992)]; [Sutherland & Peltier (1995)]). We note that although the basic state Brunt-Väisälä profile has only a smooth doubling at the jet levels, the time-varying mean state, in our DNS, evolves to a profile having such a N^2 notch.

[Nastrom & Eaton (1997)] found a localized decrease of N^2 at the tropopause level in several winter seasonal profiles, which adds credence to our simulation results (cf. their Fig. 5b). The vertical profiles of the gradient Richardson number $Ri_g = N_{eq}^2 / (\partial \bar{U} / \partial z)^2$ at the quasi-equilibrium are shown in figure 10b for cases 1, 2 and 3. Here $N_{eq}^2 = Nd(\vartheta)/dz + N^2 K^2(z)$ are the normalized Brunt-Väisälä frequency profiles at quasi-equilibrium. The gradient Richardson number Ri_g profile at quasi-equilibrium is very similar to those obtained by [Bedard, Canavero & Einaudi (1986)] as shown in figure 3a and to the profiles for cases 4, 5 and 6 in figure 3b. Comparing cases 1, 2 and 3, we can see that an increase of stratification causes the curves of Ri_g to move closer to the core. On the other hand, increase or decrease in the forcing term also changes the vertical position of the Ri_g curves, which is clear when we compare cases 1 and 5.

Visualizations of the flow fields are shown in figures 11-14 for a better understanding of the flow structure. The velocity vectors, fluctuation temperature, spanwise vorticity and local gradient Richardson number on a typical vertical plane cross-section (where the horizontal scale is taken to be αx) are plotted here for cases 1 and 2. As can be seen in figure 11a, Kelvin-Helmholtz type instability at the edges of the jet produces counterclockwise flow on top and clockwise flow on the bottom. This agrees with the contour levels of the spanwise vorticity in figure 12a. Entrainning fluid from above and below the jet generates fingers of hot and cold fluid, as evident from temperature contours shown in figure 11b. The temperature fluctuation at the center is comparatively small. Figure 12b shows the local gradient Richardson number at the same vertical plane cross-section. High values are obtained away from the core while values close to the center are small. The action of gravity waves propagating away from the jet stream leads to enhanced thermal fluctuations at other vertical levels. Peaks of temperature variance (see also figure 18) are shifted relative to peaks of velocity variances shown in figures 15-16. These phenomena have been observed in the atmospheric measurements by [Nastrom, Gage & Ecklund (1986)].

The fields for case 2 are plotted in figures 13 and 14 (stronger background stratification compare to case 1). The vortices and the waviness are observed in the vector projections (figure 13a). The corresponding spanwise vorticity field shown in figure 14a has high intensity zones concentrated around the center. The most significant differences between cases 1 and 2 are the amplitude of temperature fluctuations, which are intensified in case 2. The maxima and minima of temperature fluctuations in case 2 are closer to the core; that is $z\alpha \approx 2$ instead of $z\alpha \approx 5$ in case 1 (cf. figure 18a). The local gradient Richardson number shown in figure 14b is not significantly different from case 1.

The variances of the streamwise velocity, $\langle u'^2 \rangle / \bar{U}(0)^2$ are shown in figure 15. Cases 1, 3 and 5 have similar magnitudes while case 2 has the smallest normalized variance. In general, the variances show two peaks located roughly at the edges of the jet, at $z\alpha \approx \pm 0.70$ where $\partial U_b / \partial z$ is largest. This agrees with observations of [Beland (1993)] that the turbulence intensity is highest at the edges of the jet stream. The value of $\langle u'^2 \rangle / \bar{U}(0)^2$ is the lowest in case 2, and decays more rapidly away from the core due to the higher stratification. In contrast, the values for cases 1 and 3 are similar, suggesting that stratification in these cases is too low to have any significant effect on velocity variances. This is also true for cases 4 & 5. The variances of the spanwise velocity $\langle v'^2 \rangle / \bar{U}(0)^2$ are shown in figure 16. Their vertical profiles exhibit two peaks, but their magnitudes are generally much smaller than for the corresponding streamwise components. For cases 4 & 5, the values of spanwise velocity variance at the core increase as the Reynolds number increases. Typically, the spanwise component has smaller relative value in the TKE budget than the streamwise component, but, as the Reynolds number increases intercomponent energy transfer also increases, thus reducing anisotropy of the field. Vertical velocity variances $\langle w'^2 \rangle / \bar{U}(0)^2$ are presented in figure 17. They show a single peak at the center of the jet core. Again, case 2 is significantly smaller in value than cases 1 and 3, in view of increased stratification. The magnitudes for cases 4 and 5 are roughly the same as in cases 1 and 3.

The normalized temperature variances $\langle \vartheta'^2 \rangle / \bar{U}(0)^2$ shown in figure 18 indicate that temperature and vertical velocity tend to be out of phase, the former peaks where the latter drops to small values. The asymmetry in all cases are very prominent, a result of the jump in Brunt-Väisälä frequency profile at the center. As stratification decreases, the turbulence penetrates deeper into the surrounding fluid, spreading the peak of temperature variance further. In case 2, the upper peak of $\langle \vartheta'^2 \rangle / \bar{U}(0)^2$ is located at $z\alpha \approx 2.4$; in case 1, at $z\alpha \approx 5$ and in case 3 at $z\alpha \approx 8$ which are even further away from the core than the peak of $\langle \vartheta \rangle$. The vertical levels of peaks for $\langle \vartheta'^2 \rangle / \bar{U}(0)^2$ tend to vary inversely with the strength of stratification. For cases 4 & 5, the temperature variance peaks roughly at the same vertical levels as in case 1. However, the magnitude of the peaks decreases as the Reynolds number increases.

The normalized horizontal heat fluxes, $\langle u' \vartheta' \rangle / \bar{U}(0)^2$, are plotted in figure 19. They are negative immediately above the center and positive below the center. This is most prominent in case 2. This is in agreement with the previously discussed figures 11 and 13 where fingers of hot fluid are entrained into the core from above and fingers of cold fluid from below. Further away from the jet, $\langle \vartheta' u' \rangle$ changes sign again. This is caused by the counterflow which carries cooler fluid to the top and hotter fluid to the bottom, resulting in a positive and a

negative secondary peak above and below, respectively.

The vertical heat fluxes $\langle w'\vartheta' \rangle / \bar{U}(0)^2$ are plotted in figure 20. For cases 1, 2 and 3, they are all negative, confirming that the heat is moving from hotter (lighter) upper domain to cooler (heavier) lower domain (down-gradient). Counter-gradient heat flux ($\langle w'\vartheta' \rangle$ positive) has been observed in others studies only when the gradient Richardson number is relatively large ($Ri_g \approx 0.5 - 1.0$, [Gerz, Schumann & Elghobashi (1989)]). For case 3, the heat flux is almost zero at the center corresponding to the near neutral stratification. The equation (2.28) for mean temperature suggests that the mean temperature is related to the gradient of the vertical heat flux. This agrees with the fact that the peak of $\langle \vartheta' \rangle$ in each case shown in figure 9 corresponds to the maximum rate of change of $\langle w'\vartheta' \rangle$. As a result, the peak of $\langle \vartheta' \rangle$ is situated further away than the peak of $\langle w'\vartheta' \rangle$. In figure 20, the profiles of $\langle w'\vartheta' \rangle / \bar{U}(0)^2$ for cases 1, 2 and 3 are significantly different. If the profiles are not normalized (not shown here), case 2 has the largest peak at the core of the flow. When stratification decreases, the amount of heat flux at the core of the flow decreases, until it drops nearly to zero for case 3. At the same time, heat flux at the edges increases and generates two peaks at $z\alpha \approx 7$ and -6.5 in case 3. The doubling of the Brunt-Väisälä profile results in the asymmetry of the heat flux profiles.

Anisotropy in stably stratified mixing layers has been studied by [Smyth & Moum (2000)]. They found that the vorticity becomes isotropic as the Reynolds number increases. Velocity has a similar trend but it is possible that in real atmospheric situations some degree of anisotropy will be retained. Indeed, anisotropy of turbulent fields observed in stratospheric measurements is discussed in [Vinnichenko (1980)]. Recent observations of turbulence around a winter jet stream using the 'Egrett' meteorological research aircraft actually show that anisotropy persists at the smallest scale observed ($\sim 1m$) ([Cote, Roadcap, Wroblewski, Dobosy & Crawford (2003)]).

4 Variability of length scales and gradient Richardson number

The behaviour of stably stratified turbulent flows can be characterized in terms of length scales where buoyancy, shear, inertial and viscous influences become dominant or length-scale ratios that indicate the relative magnitudes of these influences. Some commonly used length-scales are the shear length scale L_s , Ellison scale L_e , buoyancy scale L_b and Ozmidov scale L_o defined in table 3. Here ϵ is the dissipation rate of turbulent kinetic energy intro-

duced in eq. (2.26). Relationships between these length scales have been investigated extensively, for example, in the atmospheric boundary layer by [Hunt, Kaimal & Gaynor (1985)], through atmospheric radar observations by [Eaton & Nastrom (1998)], in numerical simulations by [Itsweire, Koseff, Briggs & Ferziger (1993)]) and using laboratory experiments ([Rohr, Itsweire, Helland & Van Atta (1988)]; [De Silva & Fernando (1992)] (see [Fernando (2002)] for recent discussions). From these scales, several important scale ratios can be constructed. For example, the ratio $Ri_g = L_s^2/L_b^2$ already shown in figure 3b and figure 10b is the gradient Richardson number Ri_g .

Table 3: Definition of length scales.

| | streamwise | spanwise | vertical | other |
|------------------------------|--|----------|--|---|
| Kolmogorov scale, L_η^2 | - | - | - | $(\nu^3/\epsilon)^{1/2}$ |
| Shear scale, L_s^2 | $\langle u'^2 \rangle / (d\bar{U}/dz)^2$ | - | $\langle w'^2 \rangle / (d\bar{U}/dz)^2$ | $q^2 / (d\bar{U}/dz)^2$ |
| Ellison scale, L_e^2 | - | - | - | $\langle \theta'^2 \rangle / \left(\frac{\partial \bar{\theta}}{\partial z} \right)^2$ |
| Buoyancy scale, L_b^2 | - | - | $\langle w'^2 \rangle / N_{eq}^2$ | q^2 / N_{eq}^2 |
| Ozmidov scale, L_o^2 | - | - | - | ϵ / N_{eq}^3 |

Body forces, such as background buoyancy, typically tend to influence motion scales that are larger than certain ‘outer’ scales (Ozmidov, buoyancy, Ellison and shear). The scales of active Kolmogorov turbulence are those scales which are greater than the Kolmogorov scale but smaller than any outer scale. [Ozmidov (1965)] suggested that buoyancy effects are important on a scale proportional to L_o defined in table 3. The Ozmidov scale is regarded as the outer scale above which the fluid turbulence is significantly affected by buoyancy (cf. [Phillips (1972)], (1991)). Also, the dynamics of a stably stratified turbulent flow depend on the rate at which fluid elements mix with each other and change their density in the interior of the flow. [Ellison (1957)] introduced the scale L_e now known as the overturning or Ellison scale which uses the density (temperature) fluctuations as an indicator of the vertical scale turbulent motions; L_e is a typical vertical distance traveled by fluid particles before either returning towards their equilibrium level or mixing ([Rohr, Itsweire, Helland & Van Atta (1988)]).

The ratio $L_s/L_b = Ri_g^{1/2}$ accounts for the relative scales of influence of shear and buoyancy. If $Ri_g > 1$, then the buoyancy influence occurs at a smaller scale than the shear, and if active turbulence exists, then $\epsilon \sim (w'^2)^{3/2}/L_b$ and hence $L_b \sim (w'^2)^{1/2}/N \sim (\epsilon L_b)^{1/3}/N \sim L_o$ indicating that the Ozmidov scale L_o represents the scale beyond which the turbulent eddies

are influenced by stratification ([Fernando & Hunt (1996)]). Note that, in general, L_o should be contrasted from the buoyancy scale L_b at which the fluid parcel displacements (either due to turbulence or waves) are constrained by the buoyancy forces. The Kolmogorov scale L_η characterizes the smallest scale of active turbulence and $L_o \sim L_\eta$ then characterizes the complete suppression of active turbulence by stratification, leading to states with significant wave activity. The Ellison scale L_e is representative of the vertical motions of a stratified turbulent fluid, in that it specifies how fluctuations associated with such motions (due to eddies or waves or combination thereof) are related to the vertical scale of motions. Given that both L_b and L_e respond to the presence of waves and turbulence alike, [Hunt, Kaimal & Gaynor (1985)] have suggested that the ratio L_e/L_b , which is called the temperature fluctuation parameter, is insensitive to the presence of waves, with an estimated value of $L_e/L_b = 1.0 \pm 0.5$. For the weakly stable case of $Ri_g < 1$ with intense turbulence, the Ozmidov scale has a limited significance and large L_o/L_b values are possible.

In figures 21a,b three length scales L_o , L_e and L_η are compared for cases 1 and 2, respectively. The scales are normalized by $1/\alpha$, and for the sake of clarity their logarithmic values are shown; note the difference in vertical variability of different length scales. While L_e and L_o are bell shaped and peak roughly at the jet core, L_η becomes minimum therein. Ozmidov and Kolmogorov scales differ significantly in the core indicating active turbulence with strong mixing, concurrent with the low Ri_g values in the core (figure 10b). The ratio of L_o/L_η decreases markedly along the jet edges, indicating increased inhibition of mixing and impact of buoyancy on much smaller scales. Beyond $z\alpha \approx \pm 6$, the turbulent fluctuations die down (figures 15-18), so as the vertical heat flux (figure 20). The scales L_e and L_o in the upper domain drop faster than in the lower domain because of higher stratification. Figure 21b is a plot of length scales for case 2, which is generally similar to case 1. The Kolmogorov scale remains unchanged, but two peaks of L_o can be seen in the jet shear layers. However, the levels where $L_\eta \approx L_o$ and $L_\eta \approx L_e$ now occurs at a much lower vertical levels $z\alpha \approx \pm 3$, a signature of decreased spatial influence of jet due to increased stratification. These observations are consistent with the fields shown in figures 11-14. The decades of separation between L_η and the outer scales in the zone of active turbulence do guarantee the effective resolution of all scales. For case 2, figure 21b, L_e becomes greater than L_o for $z\alpha > 2$ (the ratio L_e/L_o crosses unity at $z\alpha \approx 2$); from figure 10b these are also the vertical levels where $Ri_g > 0.25$, with pronounced temperature fluctuations and very patchy turbulence in that region. This is in general agreement with figure 10 of [Schumann & Gerz (1995)] who have plotted ratios of L_e/L_o vs Richardson number and observed $L_e/L_o < 1$ for Ri_g small, and $L_e/L_o \approx 1$ at $Ri_g \approx 0.25$ (in the context of uniform linear vertical shear and stratification).

Figures 22 a,b show the variations of L_o , L_b and L_s for cases 1 and 2, respectively. In figure 22a, within the jet core $|z\alpha| < 2$ (except at the center) $L_s \ll L_b$, indicating a low Ri_g ($\ll 1$) conditions prone for instabilities and turbulence. In the core $L_o \gg L_s$, and somewhat larger than L_b indicating that turbulence in this region is active and intense. Note that $L_s < L_b$ implies that the vertical fluid particle displacements are sufficiently large to be deformed by the mean shear, promoting the interaction between Reynolds stresses and mean shear to yield sustained turbulence in the core ($|z\alpha| < 2$), which is clear from figures 15-19. In figure 22b which has higher stratification than case 1 we have $L_o < L_b$ throughout the vertical profile, indicating prominent wave activity.

Since Ri_g is small (< 0.25) in the jet core (except the center $z\alpha = 0$), the turbulence therein is intense and the temperature is well mixed, leading to low temperature fluctuation levels in the core (figures 3b, 11b, 18). In the higher Ri_g region where buoyancy-dominated turbulence prevails, temperature fluctuations become maximum, thus providing conditions for higher optical turbulence. This is a region of interest where the length scale ratio $L_o/L_b < 1$ points to significant wave activity (figure 24a). Detailed energy budgets (see Section 5; figures 25-26) show that in this region the shear production is vanishing and the energy is received via energy transfer from the jet core region. However, the energy deposited in this region by the pressure-velocity term is much smaller (and sometime negative) than that gained by the nonlinear terms, the wave activity appears to be dominated by non-linear waves. Given that the wave energy does not propagate beyond $|z\alpha| \approx 6$, it appears that these non-linear waves break and cause intermittent turbulent patches in the region ($2 < |z\alpha| < 6$), which is consistent with the high local Ri_g regions of figures 12b and 14b. Such breaking events can sustain some heat flux (as shown in figures 19-20) in this layer while maintaining high temperature fluctuations.

At the edges of the jet (case 1, figure 22a), in a thin layer around $|z\alpha| \approx 1.8$, we have $L_s > L_o, L_b$ indicating that the turbulence production by shear and Reynolds stress interaction is impeded. Ri_g in this region is large (figure 3b) and hence the active turbulence is possible when Ri_g locally drops below a critical value (0.25) to produce Kelvin-Helmholtz type instabilities. Figures 11-14 show that indeed the turbulence is intermittent at the jet edges and Kelvin-Helmholtz type instabilities are present. At larger distances from the jet center $2.2 < |z\alpha| < 4$, $L_b \sim L_s$, indicating marginal conditions for the maintenance of stratified turbulence; figure 12 shows that turbulence in this region is very patchy. Also, pronounced temperature fluctuations in this region (with $L_e > L_o$ for case 2) points to possible wave activity. For $|z\alpha| > 4$, the scales L_o and L_b are markedly smaller than L_s , confirming the lack of sustained turbulence when shear is negligible. This is generally consistent with

figures 11-14 and velocity variances shown in figures 15-17.

Other length scale ratios are also of interest. As stated above [Hunt, Kaimal & Gaynor (1985)] predicted L_e/L_b ratio of unity in stable atmospheric boundary layers, and found a ratio of about 0.8 in their field measurements. The ratios of L_e/L_b in our DNS for cases 1, 2, 4 and 5 are plotted in figure 23a. The ratio is smallest around the center of the jet and increase at the edges. It drops to 0.1 at the center for case 1. In the core, L_e/L_b for case 2 (with strong stratification) is higher (≈ 0.25) than that of case 1 indicating that turbulence is more buoyancy influenced. At the center, the ratios for cases 4 and 5 are even smaller than case 1. For all cases, the ratios increase close to unity away from the core, indicating the increasing importance of wave-turbulence activities at such vertical levels. In case 2, the ratio approaches a peak value of unity at around $z\alpha \approx \pm 4$, while for cases 1, 4 and 5, the peaks of L_e/L_b are observed at $z\alpha \approx \pm 6$. From figure 18, these peaks approximately correspond to the observed peaks of $\langle \theta'^2 \rangle$ for both cases 1 and 2. Higher stratification pushes the vertical peak levels of the ratio closer to the core.

There are other methods to determine the generation of waves from jet turbulence. For example, using linear equations, [Stewart (1969)] suggested that the phase spectra of w is 90^0 ahead of ϑ if the motion is wave-like. The method was used by [Lienhard & Van Atta (1990)] but they did not obtain conclusive results. Another method is the ‘penetration condition’ derived and used by [Sutherland & Peltier (1993)], (1995) also from linearized equations. In the two-dimensional context, they used the method to demonstrate the generation of internal gravity waves from a jet profile very similar to ours. The Brunt-Väisälä profile was twice larger in the upper domain than in the lower domain with a notch at the center. In their simulations, the absolute magnitude of penetration ratio is greater than unity, the peak of the Reynolds stress moves up the domain as time evolves, suggesting the presence of linear gravity waves. If the penetration ratio were smaller than unity, the peak should also travel upward, but they find a significantly smaller magnitude. They attribute this discrepancy to nonlinear effects. The simulations were done in a 2D decaying context. In our simulations, we cannot reproduce the upward motion of the Reynolds stress peaks (in quasi-equilibrium state) and it is not certain whether similar results can be obtained in a 3D context. Nevertheless, our results, which use vertical variability of L_e/L_b as an indicator of wave activity, corroborate their findings. Remarkably, the curves for L_e/L_b show little variation for cases 4, 5 and 6 (figure 23b), and saturate with increased resolution; vertical resolution doubles from cases 4 and 5 (512 vertical levels) to case 6 (1024 vertical levels). This guarantees that our resolution of the outer scales is grid independent and physically significant.

Figure 24a shows the ratio of L_o/L_b , which is an indicator of the levels of turbulence and waves. When $L_o/L_b < 1$, the waves activity is considered prominent over turbulence and vice versa. Note how this ratio changes over the vertical spread of the jet. The value of $L_o/L_b \sim 1$ observed outside the jet core in the shear layer is of the same order of magnitude as that measured by [Hebert, Moum, Paulson & Caldwell (1992)] in a turbulent patch in Pacific equatorial (jet-like) undercurrent.

The ratio $(L_o/L_e)^{2/3}$ is sometimes called the turbulent Froude number, Fr_t and is an alternative to the bulk Richardson number ([Shih, Koseff, Ferziger & Rehmann (2000)]). Fr_t for cases 1, 2, 4 and 5 are plotted in figure 24b. The curves are bell shaped, with cases 4 and 5 having the largest values, followed by case 1 and then case 2. The values at the core are all larger than unity, but Fr_t drops to less than unity in regions where the stratification is dominant. In laboratory grid-generated, salt-stratified turbulence, [Rohr, Itsweire, Helland & Van Atta (1988)] have measured the ratio L_e/L_o from which the corresponding turbulent Froude numbers Fr_t can be deduced. For $N = 0.96$, they obtain values from 0.1 to 1.8 as the downstream position increases, which correspond to $(L_o/L_e)^{2/3}$ values of 4.6 to 0.68. Their values are in the same range as those depicted in figure 24b.

5 Budgets

Budget terms were computed in the quasi-equilibrium state in order to characterize turbulent transport processes occurring at various vertical levels. Our budget equations presented in this section are based on the decomposition of velocity, temperature and pressure fields into the mean (horizontally averaged) and fluctuating components u' , v' , w' , θ' and p' . This decomposition is given by eqs. (2.6)-(2.10). The budget equations (5.29)-(5.32) are obtained after substitution of the decomposition (2.6)-(2.10) into the governing equations and performing operations of horizontal averaging $\langle \cdot \rangle$. More discussions of the budget equations based on the decomposition (2.6)-(2.10) can be found in [Stull (1988)]. We report the budget terms of $\langle u'^2 \rangle$, $\langle v'^2 \rangle$, $\langle w'^2 \rangle$ and $\langle \vartheta'^2 \rangle$ for case 2 (high stratification), where the heat flux is larger compared to other terms.

The budget equation for $\langle u'^2 \rangle$ is :

$$\frac{\partial}{\partial t} \langle u'^2 \rangle = I_{\langle u'^2 \rangle} + II_{\langle u'^2 \rangle} + III_{\langle u'^2 \rangle} + IV_{\langle u'^2 \rangle} \quad (5.29)$$

where

$$I_{\langle u'^2 \rangle} = -2\nu \langle \nabla u' \cdot \nabla u' \rangle,$$

$$\begin{aligned}
II_{\langle u'^2 \rangle} &= 2\langle p' \frac{\partial u'}{\partial x} \rangle, \\
III_{\langle u'^2 \rangle} &= \frac{\partial}{\partial z} (\nu \frac{\partial}{\partial z} (\langle u'^2 \rangle) - \langle w'u'^2 \rangle), \\
IV_{\langle u'^2 \rangle} &= -2\langle u'w' \rangle \frac{\partial}{\partial z} \bar{U}.
\end{aligned}$$

The budget terms are normalized by the quantity $U(0)^3 \alpha$. The normalized terms for $\langle u'^2 \rangle$ are plotted in figure 25a for the strongly stratified case 2. The only source term is the shear production ($IV_{\langle u'^2 \rangle}$). It has two peaks, located on either side of the model jet stream, in agreement with the graph of $\langle u'^2 \rangle$ in figure 15. The energy produced is either dissipated or transferred to other components through the dissipation ($I_{\langle u'^2 \rangle}$) and pressure redistribution ($II_{\langle u'^2 \rangle}$) terms. The pressure term also consists of two peaks directly opposite to the peaks of the production terms. This term is effective in transferring energy from the streamwise direction and depositing it to the spanwise and vertical directions. The dissipation term has the largest values at the center, and it decreases away from the center. The transport term ($III_{\langle u'^2 \rangle}$) moves energy from the peaks to the center and a lesser amount to the outer edges of the jet.

The budget equation for the spanwise velocity is :

$$\frac{\partial}{\partial t} \langle v'^2 \rangle = I_{\langle v'^2 \rangle} + II_{\langle v'^2 \rangle} + III_{\langle v'^2 \rangle} + IV_{\langle v'^2 \rangle}, \quad (5.30)$$

where

$$\begin{aligned}
I_{\langle v'^2 \rangle} &= -2\nu \langle \nabla v' \cdot \nabla v' \rangle, \\
II_{\langle v'^2 \rangle} &= 2\langle p' \frac{\partial v'}{\partial y} \rangle, \\
III_{\langle v'^2 \rangle} &= \frac{\partial}{\partial z} (\nu \frac{\partial}{\partial z} (\langle v'^2 \rangle) - \langle w'(v'^2) \rangle), \\
IV_{\langle v'^2 \rangle} &= -2\langle v'w' \rangle \frac{\partial}{\partial z} \bar{V}.
\end{aligned}$$

The budget terms for $\langle v'^2 \rangle$ are shown in figure 25b. The source is the pressure ($II_{\langle v'^2 \rangle}$) which transfers energy from the streamwise to the spanwise direction. The magnitude of the pressure term is small compared to the similar term in the budget equation for the vertical velocity (figure 26a). The dissipation term ($I_{\langle v'^2 \rangle}$), in contrast to the streamwise component, has two side peaks. The transport term ($III_{\langle v'^2 \rangle}$) moves energy from either side to the center and away from the jet. The shear production term $IV_{\langle v'^2 \rangle}$ in the spanwise direction is small compared to other terms.

The budget equation for the vertical velocity is:

$$\frac{\partial}{\partial t} \langle w'^2 \rangle = I_{\langle w'^2 \rangle} + II_{\langle w'^2 \rangle} + III_{\langle w'^2 \rangle} + IV_{\langle w'^2 \rangle}, \quad (5.31)$$

where

$$\begin{aligned} I_{\langle w'^2 \rangle} &= -2\nu \langle \nabla w' \cdot \nabla w' \rangle, \\ II_{\langle w'^2 \rangle} &= 2 \langle p' \frac{\partial}{\partial z} w' \rangle, \\ III_{\langle w'^2 \rangle} &= \frac{\partial}{\partial z} (\nu \frac{\partial}{\partial z} \langle w'^2 \rangle - \langle w'^3 \rangle - 2 \langle p' w' \rangle), \\ IV_{\langle w'^2 \rangle} &= 2N \langle w' \vartheta' \rangle. \end{aligned}$$

The budget terms for $\langle w'^2 \rangle$ are shown in figure 26a. The pressure redistribution term ($II_{\langle w'^2 \rangle}$) takes a larger portion of energy from the streamwise direction than the spanwise term $II_{\langle v'^2 \rangle}$. The energy is then either dissipated ($I_{\langle w'^2 \rangle}$) or converted to potential energy through the buoyancy term ($IV_{\langle w'^2 \rangle}$). The dissipation term here has magnitude similar to that in the spanwise direction; but this term is now dominant at the center. The transport term ($III_{\langle w'^2 \rangle}$) plays a more significant role than in the spanwise direction, in that it transports energy from the jet shear layer area to the outer region (which may be responsible for the intermittent wave breaking activity seen in figures 13-14). The buoyancy term is negative and heat flux is thus down gradient (from hot to cold). No counter gradient heat flux was observed from the equilibrium statistics (figure 20).

The budget equation for the temperature is :

$$\frac{\partial}{\partial t} \langle \vartheta'^2 \rangle = I_{\langle \vartheta'^2 \rangle} + II_{\langle \vartheta'^2 \rangle} + III_{\langle \vartheta'^2 \rangle}, \quad (5.32)$$

where

$$\begin{aligned} I_{\langle \vartheta'^2 \rangle} &= -2\kappa \langle \nabla \vartheta' \cdot \nabla \vartheta' \rangle, \\ II_{\langle \vartheta'^2 \rangle} &= -2 \langle w' \vartheta' \rangle \left(NK^2 + \frac{\partial}{\partial z} \langle \vartheta' \rangle \right) = -2 \langle w' \vartheta' \rangle \frac{N_{eq}^2}{N}, \\ III_{\langle \vartheta'^2 \rangle} &= \frac{\partial}{\partial z} (\kappa \frac{\partial}{\partial z} \langle \vartheta'^2 \rangle - \langle w' \vartheta'^2 \rangle). \end{aligned}$$

The budget terms for $\langle \vartheta'^2 \rangle$ are shown in figure 26b. The gradient production term ($II_{\langle \vartheta'^2 \rangle}$) is the only source in the balance of potential energy. It has a peak above $z\alpha \approx 2$ where the buoyancy flux for case 3 is larger. The dissipation term ($I_{\langle \vartheta'^2 \rangle}$) has roughly the same shape as the production term but, of course, with the opposite sign. This may explain why countergradient fluxes are not observed in figure 26a; temperature anomalies

dissipate in the generation region, without producing restratification effects that would lead to countergradient fluxes. The transport term ($III_{\langle v' \rangle}$) is relatively small.

The normalized shear production ($IV_{\langle u' \rangle}$) in the streamwise direction for cases 1, 2 and 3 is shown in figure 27a. Cases 1 and 3 have nearly identical shear production. Case 2, which is more stably stratified, has smaller shear production at each vertical level compare to cases 1 and 3. Thus, the normalized shear production decreases with increasing stratification in our flows. This is consistent with the conclusion in [Holt, Koseff & Ferziger (1992)] that stratification does not directly reduce the growth of q^2 (i.e. not a kinetic energy sink). Rather, the effect of stratification is indirect in suppressing the production (see also [Rohr, Itsweire, Helland & Van Atta (1988)]). The normalized total dissipation ($I_{\langle u' \rangle} + I_{\langle v' \rangle} + I_{\langle w' \rangle}$) for the three cases is shown in figure 27b. The dissipation for case 2 decreases following the decrease in production. The ratio of production over dissipation is shown in figure 27c. The three curves nearly collapse into one, suggesting that production and dissipation maintain the same ratio regardless of stratification. However, the ratio changes with $z\alpha$ and peaks at the edges of the jet, where shearing is maximum, $z\alpha \approx 1$. Around the jet production and dissipation are not at equilibrium and the transport must be taken into account. Another relevant parameter is the growth parameter F as defined in [Holt, Koseff & Ferziger (1992)]

$$F = \frac{\text{production} - \text{buoyancy}}{\text{dissipation}} = \frac{|IV_{\langle u' \rangle}| - |IV_{\langle w' \rangle}|}{|I_{\langle u' \rangle}| + |I_{\langle v' \rangle}| + |I_{\langle w' \rangle}|}. \quad (5.33)$$

The dependence of F on $z\alpha$ is shown in figure 27d. It varies roughly between 0 and 2.5 depending on the vertical level. We note that F is roughly equal to unity in homogeneous simulations for critical Richardson number, e.g. [Holt, Koseff & Ferziger (1992)], and in experiments, e.g. [Strang & Fernando (2001)], suggesting that TKE transport plays a more significant role in the situations considered herein.

6 Conclusions

A spectral domain decomposition method was developed to study inhomogeneous shear-stratified turbulent flows in the ABL context with focus on the detailed structure of a turbulent jet in the tropopause region. In contrast to most previous work, the method employed here permits more realistic boundary conditions in the vertical direction and allows shear and stratification profiles to adjust during flow evolution. Quasi-equilibrium solutions were obtained via long-time integration of governing equations. In this state, the micro-scale Reynolds number and other averaged quantities fluctuate within 5 % of their mean value. In previous numerical studies, the micro-scale Reynolds number was temporally evolving

except at a certain “stationary” Richardson number.

The quasi-equilibrium jet produced during the simulations consists of a jet core surrounded by shear layers, beyond which lay a (return) counterflow. The Richardson number within the jet core is low, the Ozmidov scale is high and turbulent energy production peaks within the core, thus producing sustained turbulence. The Richardson number increases beyond the jet shear layers in such a way that the shear length-scale exceeds the buoyancy scale, thus impeding sustained energy transfer to turbulence by the mean flow. The turbulence in this region is patchy. Beyond the jet edges are regions with moderate Richardson number characterized by small Ozmidov to Buoyancy scale ratio, indicating the presence of stably stratified turbulence; the shear production rate therein is vanishingly small and the energy supply to this region occurs via propagating non-linear gravity waves (the non-linear transport term in the energy budget exceeds the pressure transport term). This is supported by a clear difference between the core and the edges of the jet with respect to the ratios of length scales. For example, the ratio L_e/L_b is significantly smaller than unity at the center while approaching unity for all cases away from the jet core, implying the increasing importance of wave activity there. This indicates that edge regions above and below the jet stream maximum shear are the regions where much of the strong interactions between the mean flow, locally generated Kelvin-Helmholtz instabilities, turbulence and propagating gravity wave instabilities take place. This is important for ABL optical propagation codes. It is also in agreement with the observational studies in [Bedard, Canavero & Einaudi (1986)] and [Dalaudier, Sidi, Crochet & Vernin (1994)].

Theoretical analysis of stratified shear flows has further established that propagating wave modes are forced at the shear layers by a Kelvin-Helmholtz type shear instability; this shear instability then supports wave radiation when the density stratification outside of the shear layer is sufficiently large ([Lott, Kelder & Teitelbaum (1992)]); this is borne out by the present simulations. Our DNS further show that with decreasing background stratification, the vertical levels of enhanced nonlinear wave interactions significantly separate away from the levels of peak shear production. Such vertical variability of turbulence statistics must be factored into ABL propagation codes and parameterizations of C_n^2 .

Our simulations were performed with lower Reynolds numbers than in the atmosphere and some of our results are effected by the low Reynolds number simulations. However, certain important properties of computed turbulent fields are not only in qualitative but also in quantitative agreement with observed geophysical flows. For example, computed ratios and variability of turbulence natural length scales (Ozmidov, buoyancy, shear and Ellison) are

broadly consistent with the observational data presented in [Bedard, Canavero & Einaudi (1986)], [Eaton & Nastrom (1998)], [Nastrom, Gage & Ecklund (1986)], [Hunt, Kaimal & Gaynor (1985)] and [Hebert, Moum, Paulson & Caldwell (1992)]. The ratios of turbulence outer scales are found to be in agreement with observations and they do not change with increasing Reynolds number and saturate with numerical resolution. This is demonstrated in figure 3b for the ratio of shear and buoyancy length scales where vertical profile of $Ri_g = L_s^2/L_b^2$ is shown for cases 4, 5 and 6 in figure 3b; and the ratios L_e/L_b for cases 4, 5 and 6 in figure 23b.

Description of turbulence and especially turbulence closure models in stratospheric layers in the ABL context require parameterizations and scaling laws for the length scales. As there are a number of different natural length scales for stably stratified turbulent flows with shear, it is not clear without additional theoretical arguments, numerical or experimental data which scales are appropriate for the present case. One of the main objectives of this research is to establish for non-homogeneous stratified shear flows in the ABL context in the vicinity of the tropopause the length scales over which different phenomena occur, their relative orders of magnitude and variability. In future work we will investigate in more depth the parameterizations for various turbulence statistics in the context of nonhomogeneous tropopausal turbulence in the ABL context to support the ABL-ADA (atmospheric decision aid).

References

- [Alisse & Sidi (2000)] ALISSE, J.-R. & SIDI, C. 2000 Experimental probability density functions of small-scale fluctuations in the stably stratified atmosphere re. *J. Fluid Mech.* **402**, 137-162.
- [Babin, Mahalov & Nicolaenko (1998)] BABIN, A., MAHALOV, A. & NICOLAENKO, B. 1998 On nonlinear baroclinic waves and adjustment of pancake dynamics. *Theoret. Comput. Fluid Dynamics*. **11**, 215-235.
- A. Babin, A. Mahalov, and B. Nicolaenko (1996a), Global splitting, integrability and regularity of 3D Euler and Navier-Stokes equations for uniformly rotating fluids, *Europ. J. of Mech., B/Fluids*, **15**, No. 3, 291-300.
- A. Babin, A. Mahalov, and B. Nicolaenko (1997a), Regularity and integrability of rotating shallow-water equations, *Proc. Acad. Sci. Paris*, **324**, Ser. 1., 593-598.
- A. Babin, A. Mahalov, and B. Nicolaenko (1997b), Global regularity and integra-

bility of 3D Euler and Navier-Stokes equations for uniformly rotating fluids, *Asymptotic Analysis*, **15**, 103–150.

A. Babin, A. Mahalov, and B. Nicolaenko (1997c), Global splitting and regularity of rotating shallow-water equations, *Eur. J. Mech., B/Fluids*, **16**, no. 1, 725–754.

A. Babin, A. Mahalov, B. Nicolaenko and Y. Zhou (1997d), On The Asymptotic Regimes and the Strongly Stratified Limit of Rotating Boussinesq Equations, *Theoretical and Computational Fluid Dynamics*, **9**, 223–251.

A. Babin, A. Mahalov, and B. Nicolaenko (1998a), On the Nonlinear Baroclinic Waves and Adjustment of Pancake Dynamics, *Theor. and Comp. Fluid Dynamics*, to appear.

A. Babin, A. Mahalov, and B. Nicolaenko (1998b), On the Regularity of 3D Rotating Boussinesq Equations, *Mathematics of Atmosphere and Ocean Dynamics*, Newton Institute Series, Cambridge University Press, to appear.

[Batchelor (1953)] BATCHELOR, G.K. 1953 Theory of homogeneous turbulence, Cambridge University Press.

[Bedard, Canavero & Einaudi (1986)] BEDARD, A.J.JR., CANAVERO, F. & EINAUDI, F. 1986 Atmospheric gravity waves and aircraft turbulence encounters *J. Atmos. Sci.* **43** 23, 2838-2844

[Beland (1993)] BELAND, R. 1993 Propagation through Atmospheric Optical Turbulence. *Atmospheric Propagation of Radiation*, F.G.Smith, Ed., SPIE Optical Engg. Press, Washington, 157-2 32.

[Carnevale, Briscoline & Orlandi (2001)] CARNEVALE, G.F., BRISCOLINE, M. & ORLANDI, P. 2001 Buoyancy to inertial range transition in forced stratified turbulence *J. Fluid Mech.* **427**, 205-239.

[Cote, Roadcap, Wroblewski, Dobosy & Crawford (2003)] Cote, O.R., Roadcap J.R., Wroblewski D.E., Dobosy R.J., and Crawford T.L., 2003: Aircraft measurements of turbulence: length scales, spectra, budgets, and the prediction problem. *12th Symp. Meteor. Observations and Instrumentation*, 83rd Amer. Meteor. Soc. Meeting, Feb. 2003, Long Beach, CA.

[Cullen (2002)] CULLEN, M.J.P. 2002 New Mathematical Developments in Atmosphere and Ocean Dynamics, and their Application to Computer Simulations *Large-scale Atmosphere-ocean Dynamics I, Analytical methods and numerical models*. Cambridge, 202-287.

[Dalaudier, Sidi, Crochet & Vernin (1994)] DALAUDIER, F., SIDI, C., CROCHET, M. & VERNIN, J. 1994 Direct evidence of "sheets" in the atmospheric temperature field *J. Atmos. Sci.* **51**, 237-248.

[De Silva & Fernando (1992)] DE SILVA, I.P.D. & FERNANDO, H.J.S. 1992 Some aspects of mixing in a stratified turbulent patch. *J. Fluid Mech.* **240**, 601-625.

[Eaton & Nastrom (1998)] EATON, F.D. & NASTROM, G.D. 1998 Preliminary estimates of the vertical profiles of inner and outer scales from White Sands Missile Range, New Mexico, VHF radar observations, *Radio Science* **33**, 895-903.

[Ellison (1957)] ELLISON, T.H. 1957 Turbulent transport of heat and momentum from an infinite rough plane, *J. Fluid Mech.* **2**, 456-466.

[Fernando & Hunt (1996)] FERNANDO, H.J.S. & HUNT, J.C.R. 1996, Some aspects of turbulence and mixing in stably stratified layers, *Dyn. of Atm. and Oceans* **23**, 35.

[Fernando (2002)] FERNANDO, H.J.S. 2002 Turbulence in stratified fluids, In *Environmental Stratified Flows*, Kluwer Academic Publishers, 163-193.

[Fornberg (1996)] FORNBERG, B. 1996 A Practical Guide to Pseudospectral Methods, Cambridge University Press.

[Galmiche, Thual & Bonneton (2002)] GALMICHE, M., THUAL, O. & BONNETON, P. 2002 Direct numerical simulation of turbulence-mean field interactions in a stably-stratified fluid. *J. Fluid Mech.* **455**, 213-242.

[Gerz, Schumann & Elghobashi (1989)] GERZ, T., SCHUMANN, U. & ELGHOBASHI, S.E. 1989 Direct numerical simulation of stratified homogeneous turbulent shear flow. *J. Fluid Mech.* **200**, 563-594.

[Grell, Dudhia & Stauffer (1995)] GRELL, G.A., DUDHIA, J. AND STAUFFER, D.R. 1995 A description of the fifth-generation Penn State/NCAR mesoscale model (MM5), NCAR/TN-398+STR, 122 pp.

[Hebert, Moum, Paulson & Caldwell (1992)] HEBERT, D., MOUM, J.N., PAULSON, C.A. & CALDWELL, D.R. 1992 Turbulence and internal waves in the equator. Part II: details of a single event. *J. Phys. Ocean.* **22**, 1346-1356.

[Herring & Metais (1989)] HERRING, J.R. & METAIS, O. 1989 Numerical experiments in forced stably stratified turbulence. *J. Fluid Mech.* **202**, 97-115.

[Holt, Koseff & Ferziger (1992)] HOLT, S.E., KOSEFF, J.R. & FERZIGER, J.H. 1992 A numerical study of the evolution and structure of homogeneous stably stratified sheared turbulence. *J. Fluid Mech.* **237**, 499-539.

[Hunt & Galmiche (2001)] HUNT, J.C.R., & GALMICHE, M. 2001 Dynamics of layers in geophysical flows. *Lecture Notes in Physics, Springer-Verlag*, **566**, 121-151.

[Hunt, Kaimal & Gaynor (1985)] HUNT, J.C.R., KAIMAL, J.C. & GAYNOR, J.E. 1985 Some observations of turbulence structure in stable layers. *Quart. J. R. Met. Soc.* **111**, 793-815.

[Itsweire, Koseff, Briggs & Ferziger (1993)] ITSWEIRE, E.C., KOSEFF, J.R., BRIGGS, D.A. & AND FERZIGER, J.H. 1993 Turbulence in stratified shear flows: implications for interpreting shear-induced mixing in the ocean. *J. Phys. Oceanog.* **23**, 1508-1522.

[Jacobitz, Sarkar & Van Atta (1997)] JACOBITZ, F.G., SARKAR, S. & VAN ATTA, C.W. 1997 Direct numerical simulations of the turbulence evolution in a uniformly sheared and stably stratified flow. *J. Fluid Mech.* **342**, 231-261.

[Kaltenbach, Gerz & Schumann (1994)] KALTENBACH, H.J., GERZ, T. & SCHUMANN, U. 1994 Large-eddy simulation of homogeneous turbulence and diffusion in stably stratified shear flow. *J. Fluid Mech.* **280**, 1-40.

[Keyser & Shapiro (1985)] KEYSER, D. & SHAPIRO, M.A. 1985 A review of the structure and dynamics of upper-level frontal zones. *Monthly Weather Review*. **114**, 452-499.

[Lienhard & Van Atta (1990)] LIENHARD, V. & VAN ATTA, C.W. 1990 The decay of turbulence in thermally stratified flow. *J. Fluid Mech.* **210**, 57-112.

[Lott, Kelder & Teitelbaum (1992)] LOTT, F., KELDER, H. & TEITELBAUM H. 1992 A transition from Kelvin-Helmholtz instabilities to propagating wave instabilities. *Phys. Fluids A* **4**, 9, 1990-1997.

[Mahalov, Nicolaenko & Zhou (1998)] MAHALOV, A., NICOLAENKO, B. & ZHOU, Y. 1998 Energy spectra of strongly stratified and rotating turbulence. *Phys. Rev. E* **57**, 5, 6187-6190.

[McWilliams, Weiss & Yavneh (1994)] MCWILLIAMS, J.C., WEISS, J.B. & YAVNEH, I. 1994 Anisotropy and coherent vortex structures in planetary turbulence *Science*. **264**, 410-413.

[Monti, Fernando, Chan, Princevac, Kowalewski & Pardyjak (2001)] MONTI, P., FERNANDO, H.J.S., CHAN, W.C., PRINCEVAC, M., KOWALEWSKI, T.A. & PARDYJAK, E.R. 2001 Observations of flow and turbulence in the nocturnal boundary layer over a slope. *J. Atmos. Sci.* **59**, 2513-2534.

[Nastrom & Gage (1985)] NASTROM, G.D. & GAGE, K.S. 1985 A climatology of atmospheric wavenumber spectra of wind and temperature observed by commercial aircraft. *J. Atmos. Sci.* **42**, 9, 950-960.

[Nastrom, Gage & Ecklund (1986)] NASTROM, G.D., GAGE, K.S. & ECKLUND, W.L. 1986 Variability of turbulence, 4-20km, in Colorado and Alaska from MST radar observations. *J. Geophys. Res.* **91**, 6722-6734.

[Nastrom & Eaton (1997)] NASTROM, G.D., AND EATON F.D. 1997: Turbulence eddy dissipation rates from radar observations at 5-20 km at White Sands Missile Range, New Mexico, *J. Geophys. Res.*, **102**, D16, 19495-19505.

[Ozmidov (1965)] OZMIDOV, R.V. 1965 On the turbulent exchange in a stably stratified ocean. *Izv. Acad. Sci. USSR. Atmos. Oceanic Phys.* **1**, 853-860.

[Pardyjak, Monti and Fernando (2002)] PARDYJAK, E.I., MONTI P. & FERNANDO, HJS 2002 Flux Richardson number measurements in stable atmospheric shear flows, *J. Fluid Mech.* **459**, 307-316.

[Phillips (1972)] PHILLIPS, O.M. 1972 Turbulence in a strongly stratified fluid-is it unstable ? *Deep Sea Res.* **19**, 79-81

[Phillips (1991)] PHILLIPS, O.M. 1991 The Kolmogorov spectrum and its oceanic cousins: a review. *Proc. R. Soc. Lond. A* **434**, 125-138

[Pope (2000)] POPE, S.B. 2000 Turbulent Flows, Cambridge University Press.

[Riley, Metcalfe & Weissman (1981)] RILEY, J.J., METCALFE, R.W. & WEISSMAN, M.A. 1981 Direct numerical simulations of homogeneous turbulence in density stratified fluids. *Proc. AIP Conf. on Nonlinear Properties of Internal Waves* **76** 79-112.

[Riley (2001)] RILEY, J.J. 2001 Dynamics of turbulence strongly influenced by buoyancy. *Environmental Fluid Dynamics Seminar*. Arizona State University.

[Rohr, Itsweire, Helland & Van Atta (1988)] ROHR, J.J., ITSWEIRE, E.C., HELLAND, K.N. & VAN ATTA, C.W. 1988 Growth and decay of turbulence in a stably stratified shear flow. *J. Fluid Mech.* **195**, 77-111.

[Schumann (1996)] SCHUMANN, U. 1996 Direct and large eddy simulations of stratified homogeneous shear flows. *Dynamics of atmospheres and oceans*. **23**, 81-98.

[Schumann & Gerz (1995)] SCHUMANN, U. & GERZ, T. 1995 Turbulent mixing in stably stratified shear flows. *J. of Applied Meteorology* **34**, 33-48.

[Shih, Koseff, Ferziger & Rehmann (2000)] SHIH, L.H., KOSEFF, J.R., FERZIGER, J.H. & REHMANN, C.R. 2000 Scaling and parametrization of stratified homogeneous turbulent shear flow. *J. Fluid Mech.* **412**, 1-20.

[Smyth & Moum (2000)] SMYTH, W.D. & MOUM, J.N. 2000 Anisotropy of turbulence in stably stratified mixing layers *Phys. Fluids*. **12**, 6, 1343-1362.

[Smyth & Moum (2002)] SMYTH, W.D. & MOUM, J.N. 2002 Shear instability and gravity wave saturation in an asymmetrically stratified jet. *Dyn. Atmos. & Ocean.* **35**, 265-294.

[Stewart (1969)] STEWART, R.W. 1969 Turbulence and waves in a stratified atmosphere. *Radio Sci.* **4**, 1269-1278.

[Strang & Fernando (2001)] STRANG, E.J. & FERNANDO, H.J.S. 2001 Entrainment and mixing in stratified shear flows. *J. Fluid Mech.* **428**, 349-386.

[Stull (1988)] STULL, R.B. 1988 Introduction to Boundary Layer Meteorology. *Kluwer Academic Publishers*.

[Sutherland & Peltier (1993)] SUTHERLAND, B.R. & PELTIER, W.R. 1993 Turbulence transition and internal wave generation in density stratified jets. *Phys. Fluids*. **6**, 3, 1267-1284.

[Sutherland & Peltier (1995)] SUTHERLAND, B.R. & PELTIER, W.R. 1995 Internal Gravity Wave Emission into the Middle Atmosphere. *J. Atmos. Sci.* **52**, 18, 3214-3234.

[Sutherland & Linden (1998)] SUTHERLAND, B.R. & LINDEN, P.F. 1998 Internal wave excitation from stratified flow over a thin barrier. *J. Fluid Mech.* **377**, 223-252.

[Tse, Mahalov, Nicolaenko & Fernando (2001)] TSE, K.L., MAHALOV, A., NICOLAENKO, B., FERNANDO, H.J.S. 2001 A spectral domain decomposition method and its application to simulations of shear-stratified turbulence . *Lecture Notes in Physics, Springer-Verlag*, **566**, 353-378.

[Vinnichenko (1980)] VINNICHENKO, N.K. 1980 Turbulence in the free atmosphere . *New York : Consultant's Bureau, c1980, 2nd edition.*

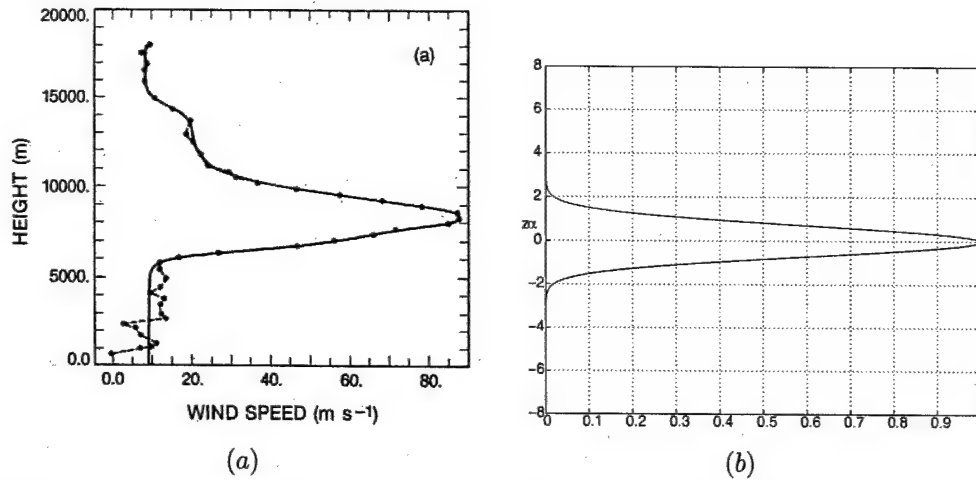


Figure 1: (a) An example of a jet stream profile from Bedard, Canavero & Einaudi (1986) (reproduced with permission from the American Meteorological Society). The dotted line is obtained from observation while the solid line is a numerical fit. (b) The normalized velocity profiles U_b at the basic state of the present computations. The vertical axis is $z\alpha$ where $\alpha = 16$, and $-8.0 \leq z\alpha \leq 8.0$. Only the middle portion of the computational box is shown here.

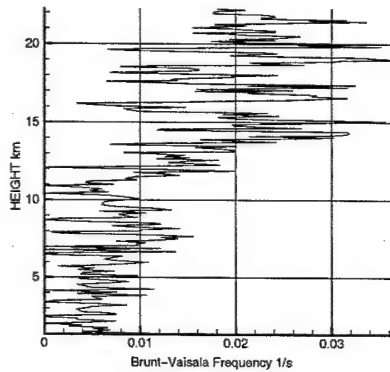


Figure 2: Brunt-Väisälä frequency profile recorded in the atmosphere by Beland (1996) with balloon measurements; vertical axis - height (km) and horizontal axis - Brunt-Väisälä frequency ($1/\text{s}$).

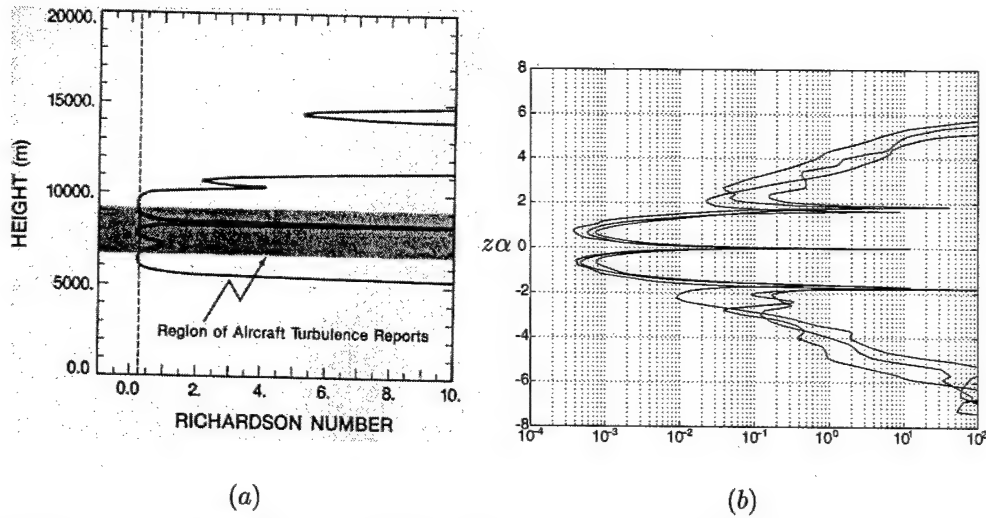


Figure 3: (a) An example of a gradient Richardson number profile corresponding to figure 1(a), measured by Bedard, Canavero & Einaudi (1986)(reproduced with permission from the American Meteorological Society); (b) Gradient Richardson number profiles at quasi-equilibrium from the numerical simulations for cases 4, 5 ($256^2 \times 512$ resolution) and case 6 ($512^2 \times 1024$ resolution).

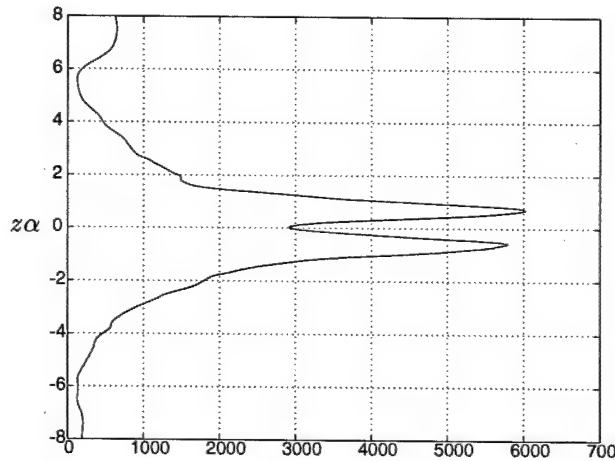


Figure 4: The Reynolds number based on the length scale L_d and q for $512^2 \times 1024$ resolution, case 6, $Re_d = qL_d/\nu$.

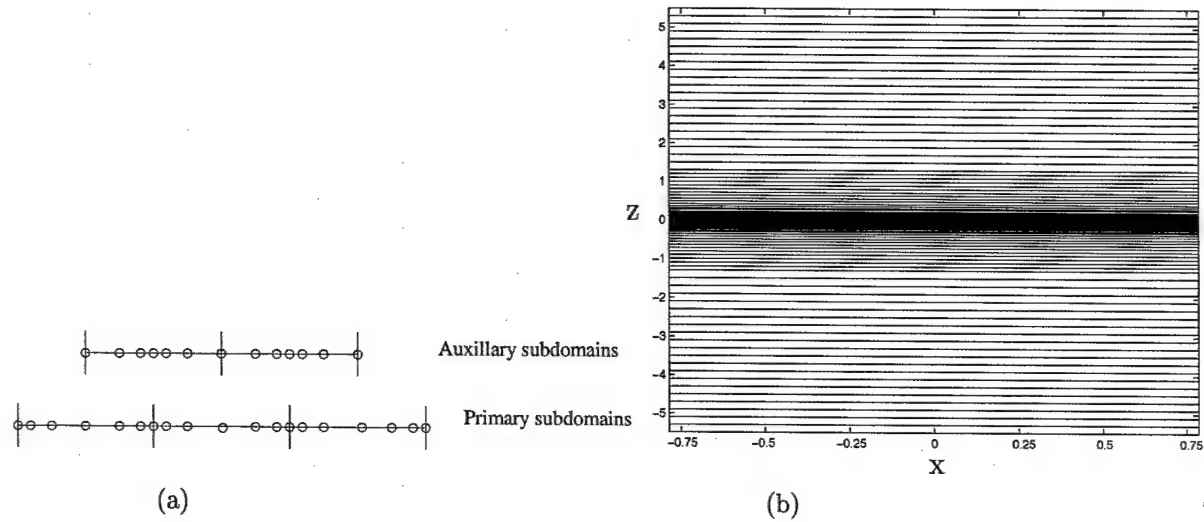


Figure 5: (a) Distribution of collocation points in primary and auxillary subdomains. The vertical lines separate the subdomains. (b) Distribution of primary subdomain boundaries in the vertical direction.

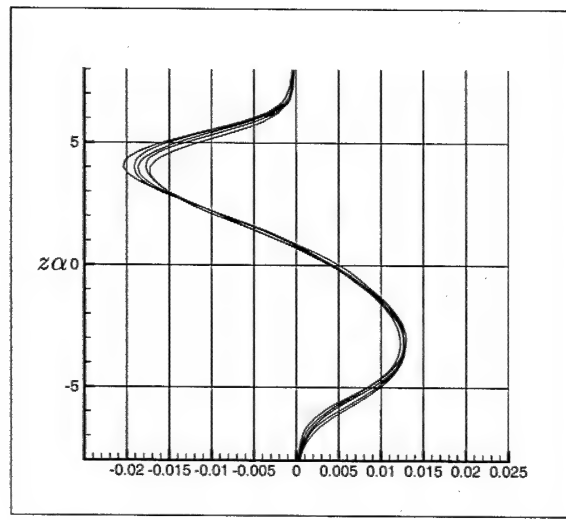


Figure 6: Evolution of the mean temperature, $\langle \vartheta \rangle$, at quasi-equilibrium, case 1.

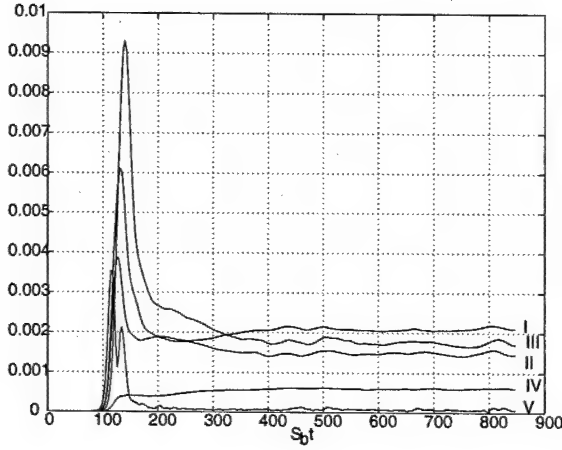


Figure 7: The time evolution of vertically integrated values of $\langle u'^2 \rangle$ (I), $\langle v'^2 \rangle$ (II), $\langle w'^2 \rangle$ (III), $\langle \vartheta'^2 \rangle$ (IV) and $|\partial \langle u'^2 \rangle / \partial t|$ (V); $\langle \cdot \rangle$ denotes horizontal averaging. Horizontal axis is given in non-dimensional time $S_b t$.

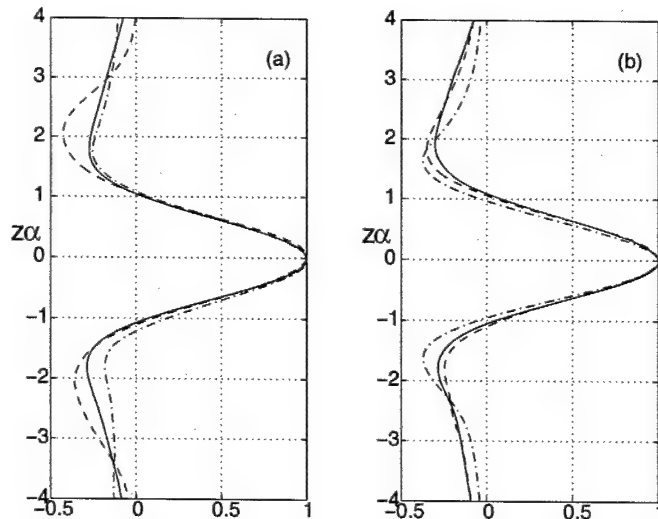


Figure 8: Normalized mean (horizontally averaged) velocity in the streamwise direction for cases listed in Table 1, horizontal axis - $\bar{U}(z)/\bar{U}(0)$ where $\bar{U} = U_b + \langle u \rangle$, vertical axis - $z\alpha$: (a) cases 1 (solid), 2 (dash) and 3 (dash-dot) ; (b) cases 4 (solid) , 5 (dash) and 6 (dash-dot).

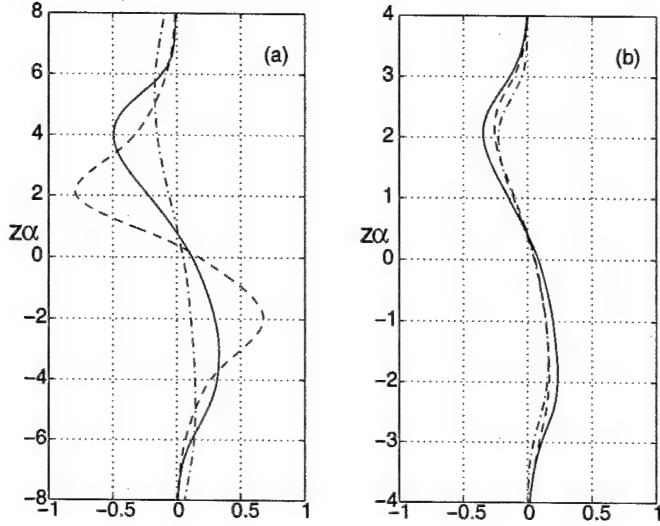


Figure 9: Normalized mean (horizontally averaged) temperature, $\langle \vartheta \rangle(z)/\bar{U}(0)$, in the quasi-equilibrium state for cases listed in Table 1, horizontal axis - $\langle \vartheta \rangle$, vertical axis - $z\alpha$; (a) cases 1 (solid), 2 (dash) and 3 (dash-dot) ; (b) cases 4 (solid), 5 (dash) and 6 (dash-dot).

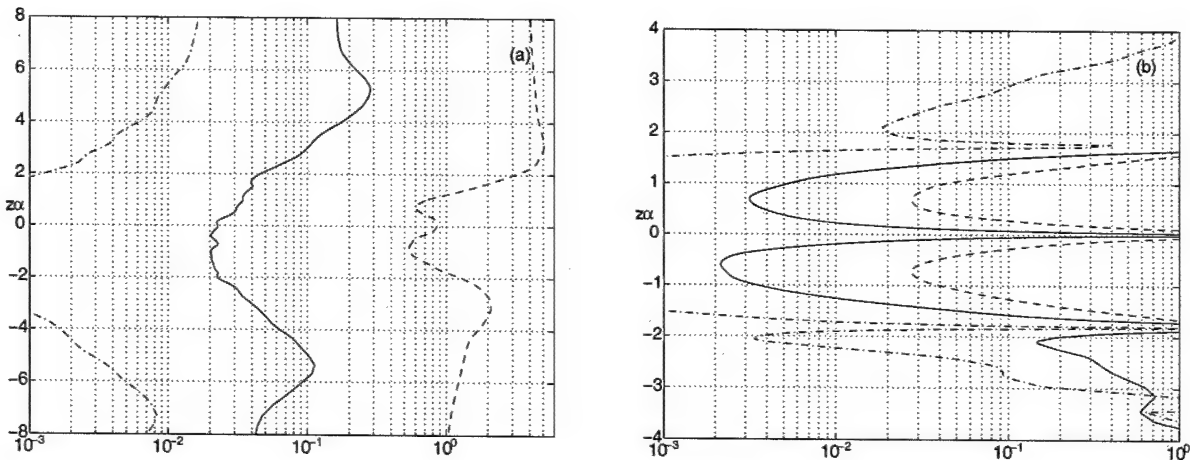


Figure 10: (a) The square of the Brunt-Väisälä frequency profile, $N^2 K^2$, and (b) Gradient Richardson number profiles at quasi-equilibrium from the numerical simulations for cases 1 (solid), 2 (dash) and 3 (dash-dot).

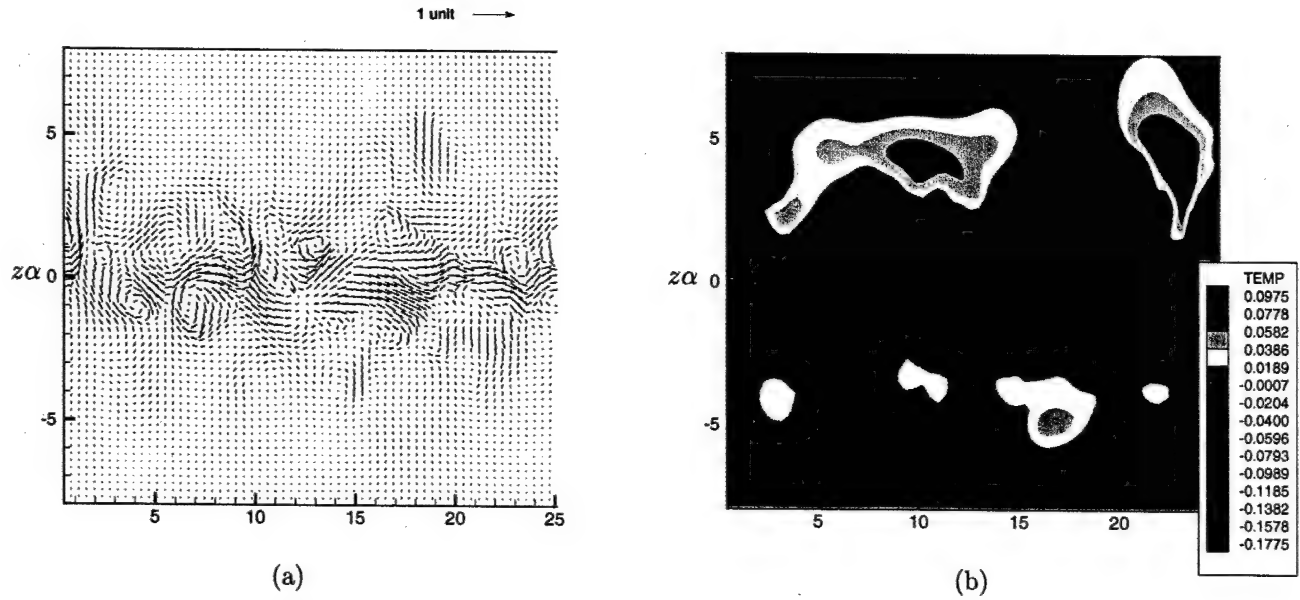


Figure 11: (a) Instantaneous velocity vectors and (b) temperature fluctuation on a vertical plane for case 1. The horizontal axis is $x\alpha$. Magnitude of velocity is given by arrow length.

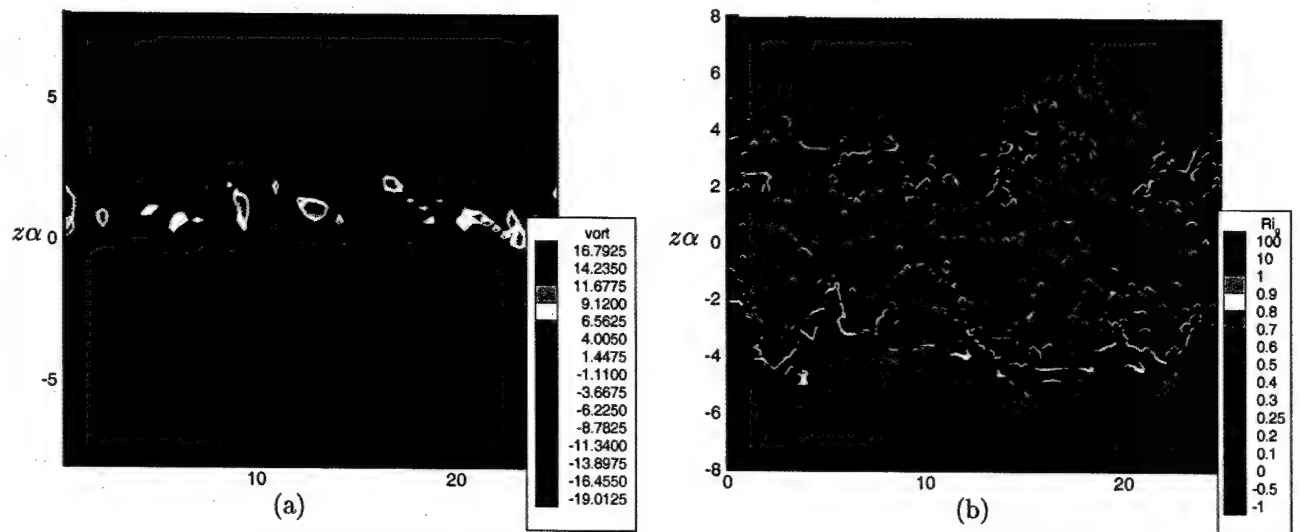


Figure 12: (a) Instantaneous spanwise vorticity and (b) local gradient Richardson number on a vertical plane for case 1. The horizontal axis is $x\alpha$.

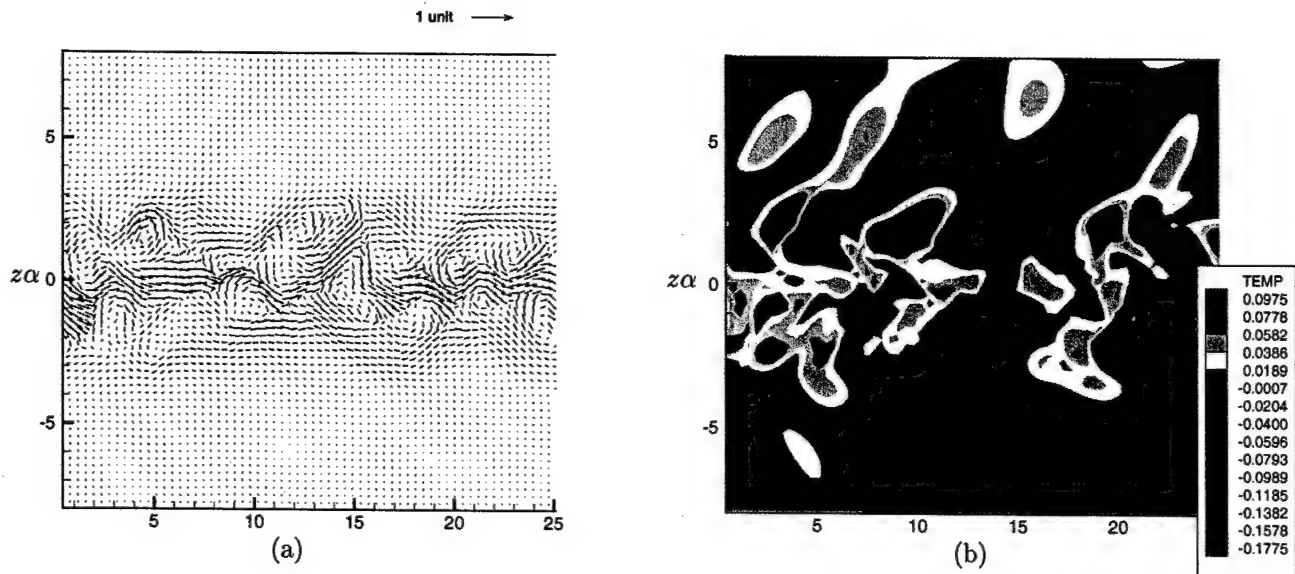


Figure 13: (a) Instantaneous velocity vectors and (b) fluctuating temperature component on a vertical plane for case 2. The horizontal axis is $z\alpha$.

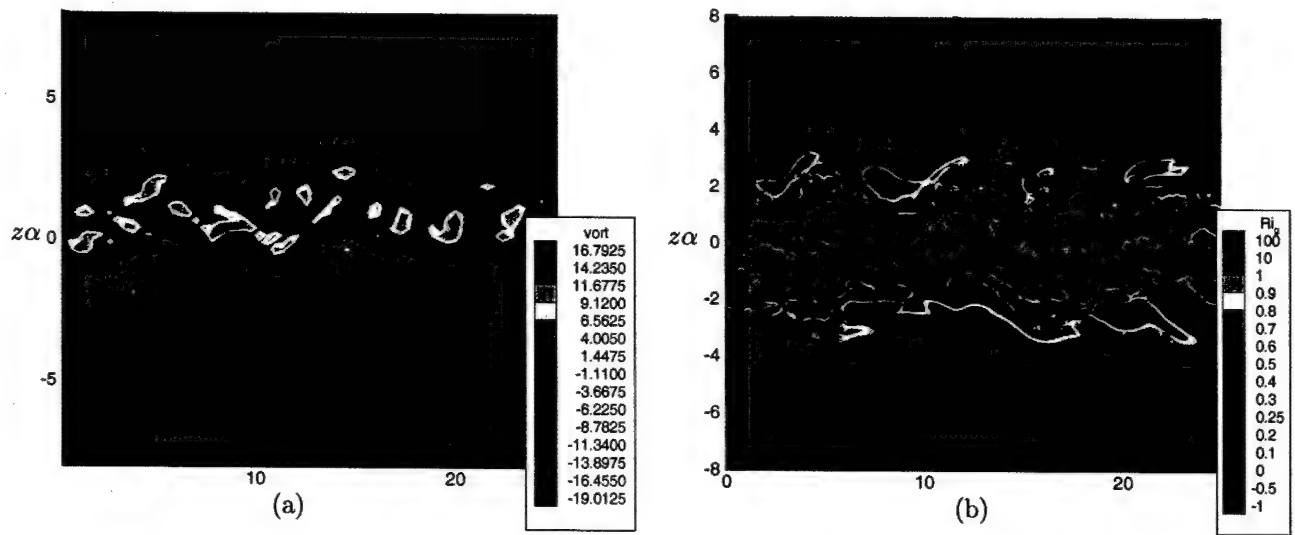


Figure 14: (a) Instantaneous spanwise vorticity and (b) local gradient Richardson number on a vertical plane for case 2. The horizontal axis is $z\alpha$.

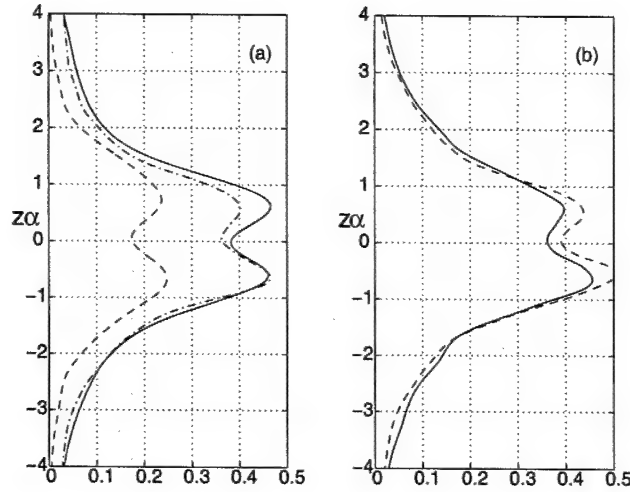


Figure 15: The normalized variances of the streamwise velocity, $\langle u'^2 \rangle / \bar{U}(0)^2$ as a function of the normalized height : (a) cases 1 (solid), 2 (dash) and 3 (dash-dot); (b) cases 4 (solid) and 5 (dash).

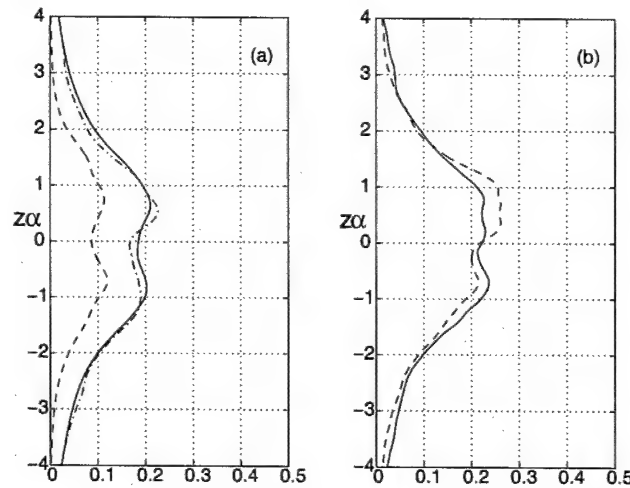


Figure 16: The normalized variances of the spanwise velocity, $\langle v'^2 \rangle / \bar{U}(0)^2$: (a) cases 1 (solid), 2 (dash) and 3 (dash-dot) ; (b) cases 4 (solid) and 5 (dash).

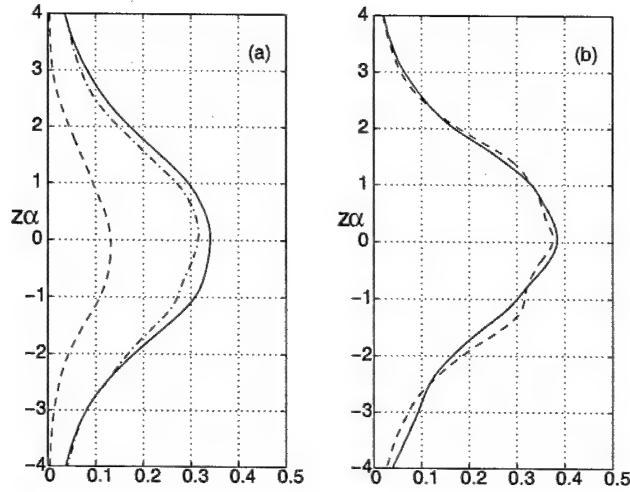


Figure 17: The normalized variances of the vertical velocity, $\langle w'^2 \rangle / \bar{U}(0)^2$: (a) cases 1 (solid), 2 (dash) and 3 (dash-dot) ; (b) cases 4 (solid) and 5 (dash).

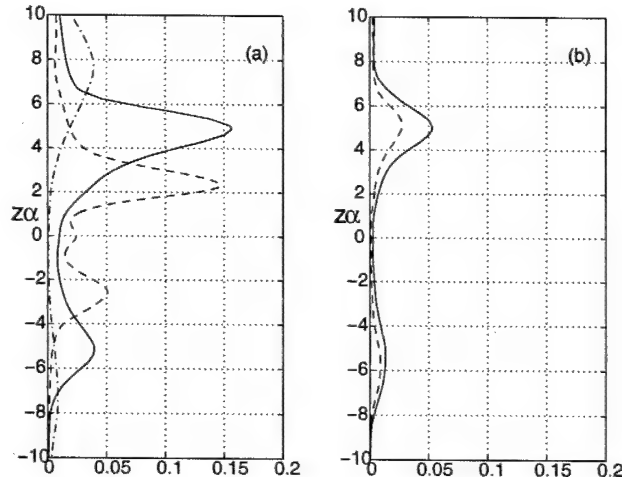


Figure 18: The normalized variances of the temperature, $\langle \vartheta'^2 \rangle / \bar{U}(0)^2$: (a) cases 1 (solid), 2 (dash) and 3 (dash-dot) ; (b) cases 4 (solid) and 5 (dash).

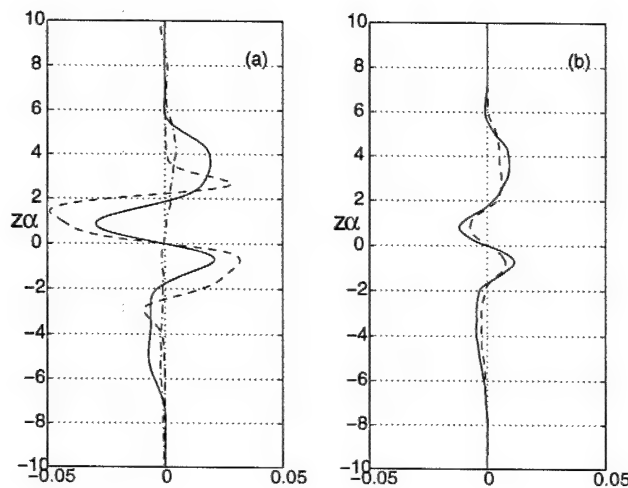


Figure 19: The normalized profile of the horizontal heat flux, $\langle \vartheta' u' \rangle / \bar{U}(0)^2$: (a) cases 1 (solid), 2 (dash) and 3 (dash-dot) ; (b) cases 4 (solid) and 5 (dash).

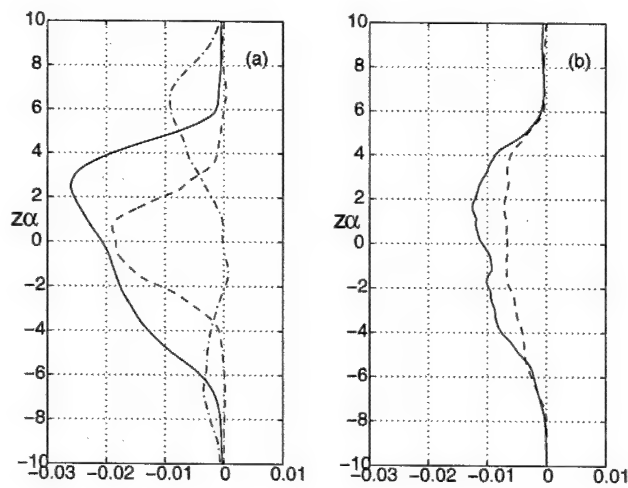


Figure 20: The normalized profile of the vertical heat flux, $\langle \vartheta' w' \rangle / \bar{U}(0)^2$: (a) cases 1 (solid), 2 (dash) and 3 (dash-dot) ; (b) cases 4 (solid) and 5 (dash).

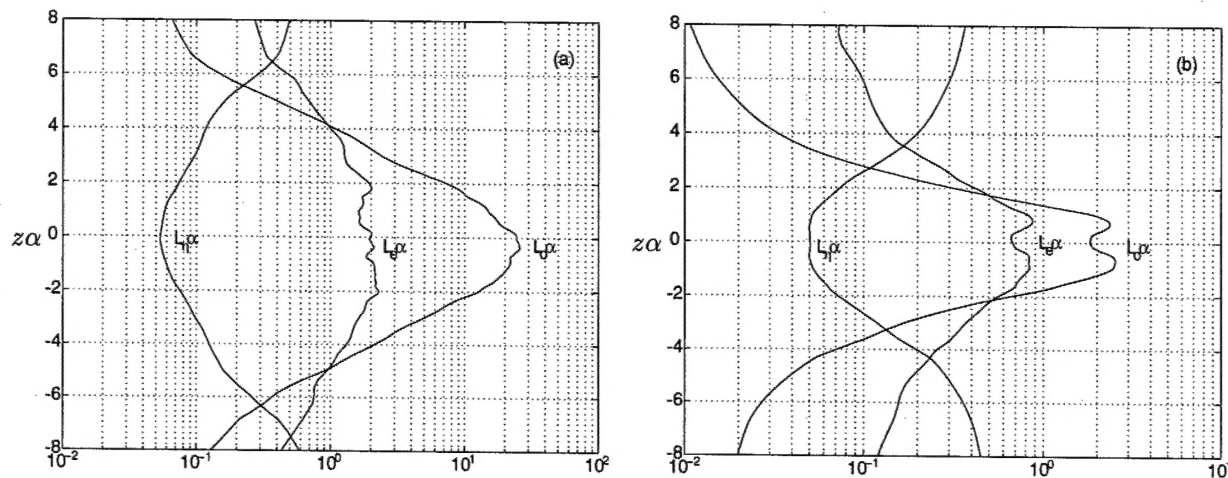


Figure 21: The normalized length scales $L_\eta\alpha$, $L_e\alpha$ and $L_o\alpha$ for (a) case 1 and (b) case 2 (logarithmic scale).

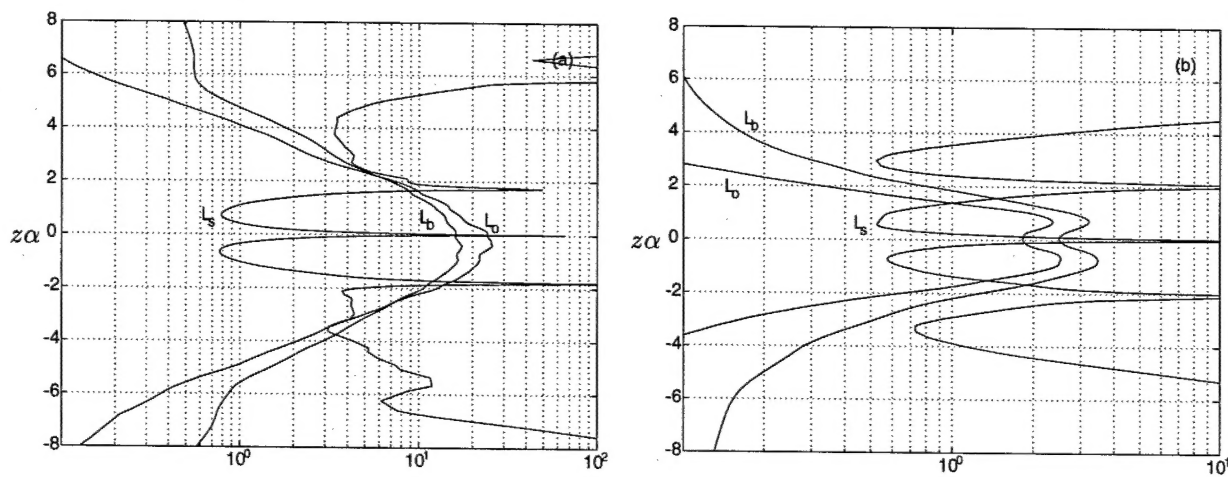


Figure 22: The normalized length scales $L_s\alpha$, $L_b\alpha$ and $L_o\alpha$ for (a) case 1 and (b) case 2 (logarithmic scale).

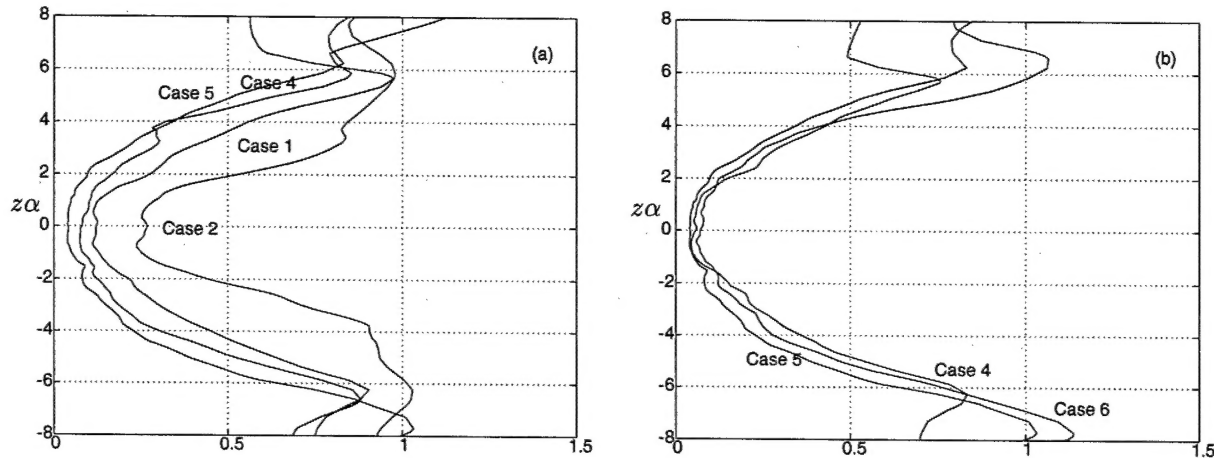


Figure 23: (a) Ratio of L_e/L_b for cases 1, 2, 4 and 5; (b) Ratio of L_e/L_b for cases 4, 5 and 6.

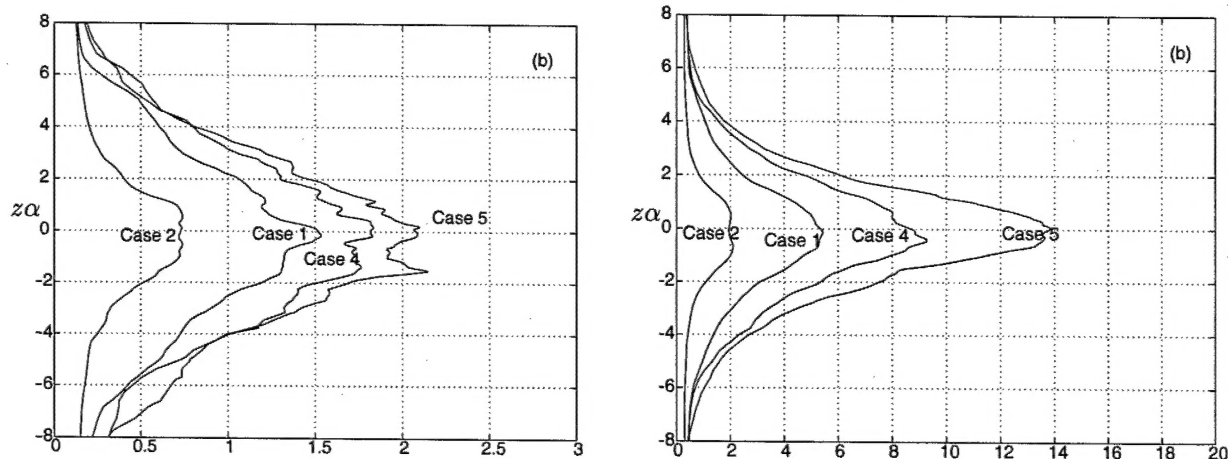


Figure 24: (a) Ratio of L_o/L_b for cases 1, 2, 4 and 5; (b) The turbulent Froude number, $Fr_t = (L_o/L_e)^{2/3}$ for cases 1, 2, 4 and 5.

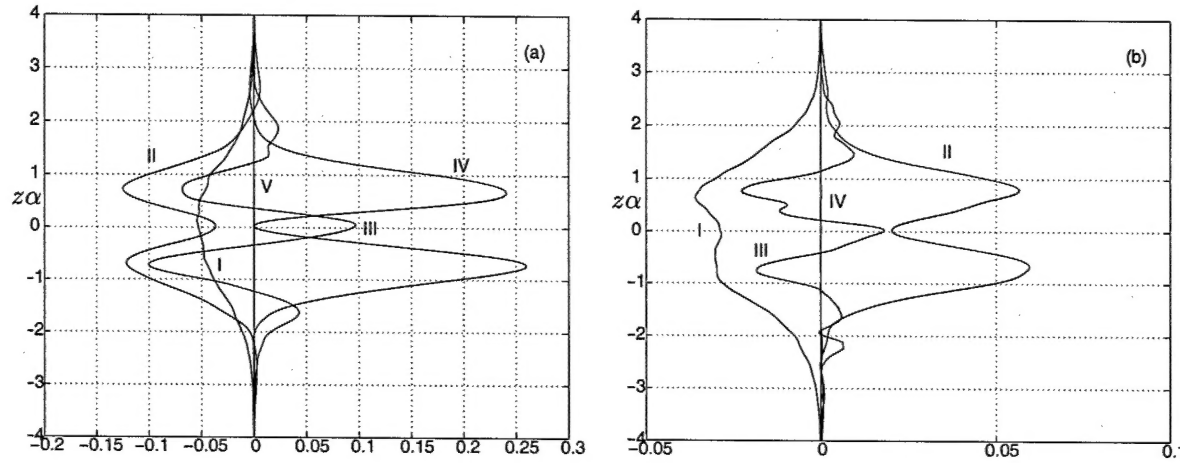


Figure 25: (a) The normalized horizontally averaged budgets in the equation for the streamwise velocity variance for case 2. Labels in the figure correspond to *I* - dissipation, *II* - pressure, *III* - transport, and *IV* - shear production. (b) The normalized budgets in the equation for the spanwise velocity variance. Labels in the figure correspond to *I* - dissipation, *II* - pressure, *III* - transport and *IV* - shear production (term *IV* is nearly zero).

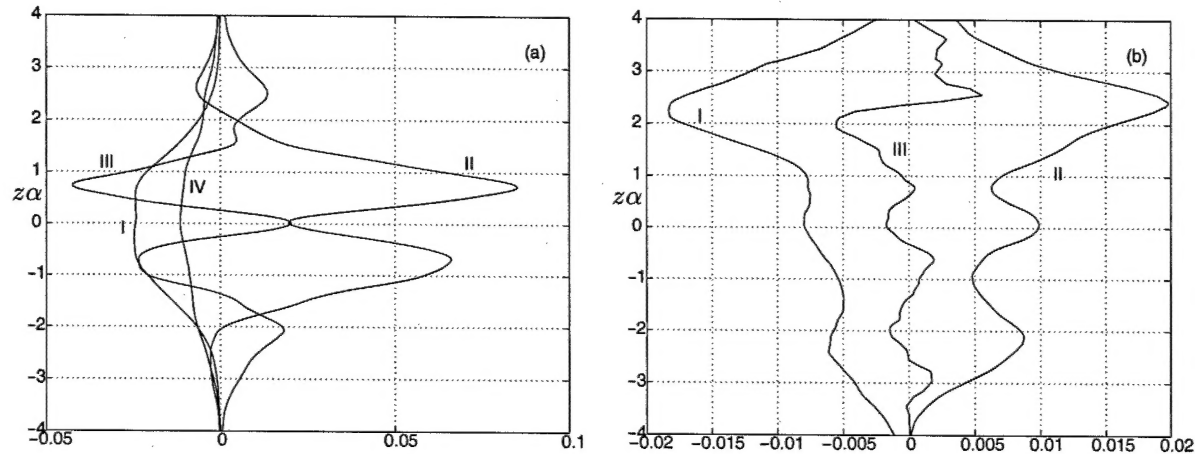


Figure 26: (a) The normalized horizontally averaged budgets in the equation for the vertical velocity variance for case 2. Labels in the figure correspond to *I* - dissipation, *II* - pressure, *III* - transport, and *IV* - buoyancy. (b) The normalized budgets in the equation for temperature variance. Labels in the figure correspond to *I* - dissipation, *II* - production and *III* - transport.

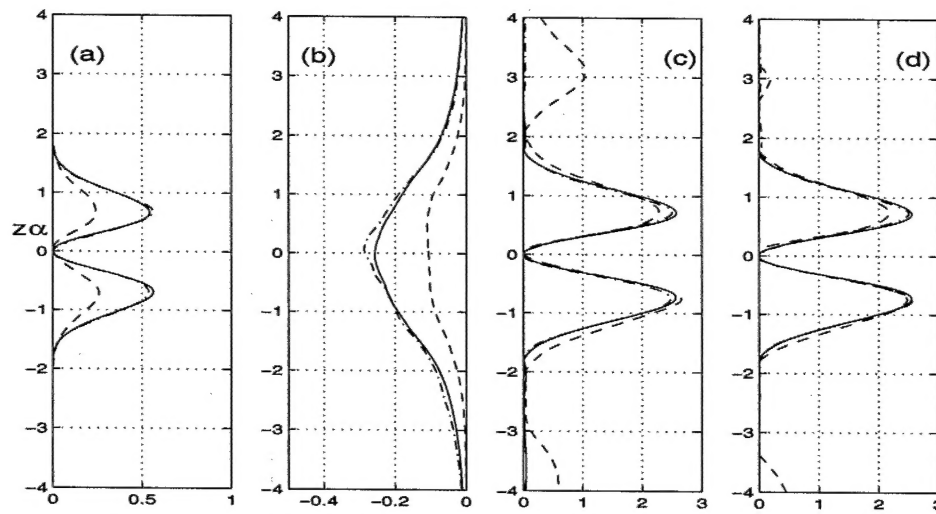


Figure 27: (a) normalized shear production; (b) normalized dissipation; (c) shear production over dissipation and (d) growth parameter for cases 1 (solid), 2 (dash) and 3 (dash-dot). Curves for cases 1 and 3 are nearly identical.